UNICAMP

UNIVERSIDADE ESTADUAL DE CAMPINAS
INSTITUTO DE FÍSICA GLEB WATAGHIN

Adimir Italo Vilca Morales

Raman Scattering Study of the Sr_2IrO_4 Iridate with Isovalent Ca and Ba Substitutions at the Sr Site

Estudo de Espalhamento Raman no Iridato Sr_2IrO_4 com substituções isovalentes de Ca e Ba no sitio do Sr

Campinas

2024

UNICAMP

Adimir Italo Vilca Morales

Raman Scattering Study of the Sr_2IrO_4 Iridate with Isovalent Ca and Ba Substitutions at the Sr Site

Estudo de Espalhamento Raman no Iridato Sr_2IrO_4 com substituções isovalentes de Ca e Ba no sitio do Sr

Dissertation presented to the ”Gleb Wataghin” Institute of Physics of the University of Campinas in partial fulfillment of the requirements for the degree of Master of Physics in the area of Physics.

Dissertação apresentada ao Instituto de Física Gleb Wataghin da Universidade Estadual de Campinas como parte dos requisitos exigidos para a obtenção do título de Mestre em Física, na Área de Física.

Supervisor: Eduardo Granado Monteiro da Silva

Este trabalho corresponde à versão final da Dissertação defendida pelo aluno Adimir Italo Vilca Morales, e orientado pelo Prof. Dr. Eduardo Granado Monteiro da Silva.

Campinas
2024

Ficha catalográfica
Universidade Estadual de Campinas (UNICAMP)
Biblioteca do Instituto de Física Gleb Wataghin
Lucimeire de Oliveira Silva da Rocha - CRB 8/9174

V711r
Vilca Morales, Adimir Italo, 1994-
Raman scattering study of the Sr_2IrO_4 iridate with isovalent Ca and Ba substitutions at the Sr site / Adimir Italo Vilca Morales. – Campinas, SP : [s.n.], 2024.

Orientador: Eduardo Granado Monteiro da Silva.
Dissertação (mestrado) – Universidade Estadual de Campinas (UNICAMP), Instituto de Física Gleb Wataghin.

1. Efeito de Raman. 2. Iridatos. I. Silva, Eduardo Granado Monteiro da, 1974-. II. Universidade Estadual de Campinas (UNICAMP). Instituto de Física Gleb Wataghin. III. Título.

Informações Complementares

Título em outro idioma: Estudo de espalhamento Raman no iridato Sr_2IrO_4 com substituções isovalentes de Ca e Ba no sitio do Sr
Palavras-chave em inglês:
Raman effect
Iridates
Área de concentração: Física
Titulação: Mestre em Física
Banca examinadora:
Eduardo Granado Monteiro da Silva [Orientador]
Túlio Costa Rizuti da Rocha
Ulisses Ferreira Kaneko
Data de defesa: 26-06-2024
Programa de Pós-Graduação: Física

Identificação e informações acadêmicas do(a) aluno(a)
- ORCID do autor: https://orcid.org/0000-0001-8044-3247
- Currículo Lattes do autor: http://lattes.cnpq.br/6127238395516822

MEMBROS DA COMISSÃO EXAMINADORA DA DISSERTAÇÃO DE MESTRADO DO ALUNO ADIMIR ITALO VILCA MORALES – RA 228219, APRESENTADA E APROVADA AO INSTITUTO DE FÍSICA GLEB WATAGHIN, DA UNIVERSIDADE ESTADUAL DE CAMPINAS, EM 26/06/2024.

COMISSÃO JULGADORA:

-Prof. Dr. Eduardo Granado Monteiro da Silva – Presidente e Orientador (IFGW/UNICAMP)

-Prof. Dr. Tulio Costa Rizuti da Rocha (Centro Nacional de Pesquisa em Energia e Materiais/Laboratório Nacional de Luz Síncrotron).

-Prof. Dr. Ulisses Ferreira Kaneko (Departamento de Física da UNESP Rio Claro).

OBS.: Ata da defesa com as respectivas assinaturas dos membros encontra-se no SIGA/Sistema de Fluxo de Dissertação/Tese e na Secretaria do Programa da Unidade.

CAMPINAS

2024

Acknowledgment

The conclusion of this period on my journey would not have happened without the support of people and institutions that helped me to rediscover and redefine my commitment to the academic work. I am therefore pleased to thank:

To Prof. Dr. Eduardo Granado, as my advisor, helped me in my learning process. In addition, he was very important in offering me the support and confidence that allowed me to complete this phase of my education.

To my small Brazilian family, Bianca, Flávia, Isadora, Rafael, Simon, Thais, Thom, who helped me feel close to my homeland.

To my parents, siblings and nephews for trusting, believing in me and also being my support.

To Ali, Carlos, Danilo, Kousik and Rodolfo for helping me integrate into IFGW and learning with each other in the Raman Laboratory. Their professionalism and companionship also helped me rebuild a model of persona for me.

To Davi, Gabriel, Isadora, Jean, Kevin, Mario and Paulo, members of the GPOMS laboratory, for the coffees and support in the development of my work.

To the University of Campinas and the Gleb Wataghin Physics Institute for the opportunity to offer me a comprehensive academic education.

To the São Paulo Rsearch Foundation - FAPESP (Grant No. 2018/18653 -4), and the National Council for Scientific and Technological Development - CNPq (Process No. 136485/2018 -9) for the financial support with a scholarship.

This study was financed in part by the Coordenação de Aperfeiçoamento de Pessoal de Nível Superior - Brasil (CAPES) - Finance Code 001

Abstract

Novel phenomena arising from the interplay of strong spin-orbit coupling and moderate electron correlations have attracted attention of the scientific community to the exotic physics presented by Sr_2IrO_4 and its family of iridates. The multiorbital character of the pseudospin $J_{eff} = 1/2$ state and the degrees of freedom of the crystal structure play a crucial role for the stabilization of its magnetic behavior. Thus, understanding the details of Sr_2IrO_4 via tunable parameters is important for a realistic description of this system. To achieve this goal, we measured with Raman spectroscopy the low-energy excitations of the system Sr_2IrO_4 under chemical pressure, obtained by isovalent substitutions at the Sr^{2+} site. Our results indicate crystal environment changes due to the chemical substitutions' impact on the spin-orbit coupled $J_{eff} = 1/2$ state, leading to an enhanced pseudospin-phonon coupling and interference between phonons and an electronic continuum. The effect of the chemical substitution onto the lattice parameters, the magnetic properties and the single magnon excitation show the important role played by the local structural distortions on the stabilization of the collective spin-orbital state $J_{eff} = 1/2$ and its long-range magnetic order.

Resumo

Novos fenômenos oriundos da combinação de um forte acoplamento spin-órbita e correlações eletrônicas moderadas chamaram a atenção da comunidade científica para a física exótica que Sr_2IrO_4 e a família dos iridatos possui. O caráter multiorbital do estado pseudospin $J_{eff} = 1/2$ e os graus de liberdade da estrutura cristalina desempenham um papel crucial para a estabilização de seu comportamento magnético. Assim, compreender os detalhes do Sr_2IrO_4 via parâmetros sintonizáveis é importante para uma descrição realista deste sistema. Com esse objetivo, medimos com espectroscopia Raman as excitações de baixa energia do sistema Sr_2IrO_4 sob pressão química, obtida por substituições isovalentes no sítio do Sr^{2+}. Nossos resultados indicam que mudanças no ambiente cristalino causadas pelas substituições químicas impactam o estado $J_{eff} = 1/2$ acoplado spin-órbita, levando a um acoplamento pseudospin-fônon aprimorado e uma interferência de fônon com o contínuo eletrônico. O efeito das substituições químicas nos parâmetros de rede, nas propriedades magnéticas e na excitação de mágnon único mostram o importante papel que as distorções locais da estrutura atômica desempenham para estabilizar o estado orbital de spin coletivo $J_{eff} = 1/2$ e sua ordem magnética de longo alcance.

List of Figures

List of Tables

Contents

Chapter 1

Introduction

Strongly correlated electronic systems have been widely explored in 3d transition metal oxides (TMOs) hosting diverse properties as high temperature superconductivity in layered cuprates and colossal magnetoresistance in perovskite manganites. These materials present a strong on-site Coulomb repulsion U between electrons that occupy the same orbital, and influencing the local moment formation and its magnetism. Then, the activity of exploring novel states of matter was expanded to the non trivial physics that comes along with strong spin-orbit coupling (SOC) including f-electron materials and more recently 4d and 5d transition metal oxides (TMOs). The strong SOC entangles the orbital momentum and spin degrees of freedom leading to a number of intriguing phenomena. Meanwhile, the electron repulsion U reduces while descending from 3d to the more extended orbitals 4d and 5d at the periodic table. The simultaneous effect of electron repulsion U and strong SOC could represent many different ground states such as topological insulators, Weyl semimetals, Fermi arc states, quantum spin liquids, etc [1, 2].

To understand materials of competing ground states, we need to consider a variety of 2D and 3D lattices crystal structures. In particular, the Ruddlesden-Popper series $Sr_{n+1}Ir_nO_{3n+1}$ has served as the most extensively studied 5d-TMOs family of materials, due to the influence of strong spin-orbit coupling and an intermediate electron correlation U. There, the strong spin-orbit coupling assists the electron correlation to open a Mott gap at the $J_{eff} = 1/2$ band [3]. Also, the similar structural, electronic and magnetic properties of the cuprate high-superconductor counterpart La_2CuO_4 have led to the expectation that Sr_2IrO_4 can become an unconventional superconductor by electron doping. However, the extensively multiorbital character of the $J_{eff} = 1/2$ state might have its own unique properties distinctive to the cuprates with weakly spin-orbit coupling, and if so, what role does strong spin-orbit coupling play in this novel phase [4].

In addition, different interactions as Jahn-Teller coupling, crystal electric field, exchange interaction, spin-orbit interaction and their hierarchy need to be better understood about how they play a crucial role to the magnetic phase and how its instability against perturbations such as magnetic field, pressure, and/or chemical substitution could result in new exotic phases [5]. Small changes in an external parameter can often lead to dramatic qualitative changes in quantum mechanical ground state of a correlated electron system. For instance, the $J_{eff} = 1/2$ pseudospin directions are nearly locked to the rotation of IrO_6 octahedra along the c-axis [6]. The cross coupling effect between collective spin and orbital ordering with the lattice degrees of freedom might have an important role in its fundamental properties to stabilize the uncommon magnetic behavior of Sr_2IrO_4. In this thesis, we tuned the Sr_2IrO_4 system with chemical pressure without electron doping in order to change bond length and/or bond angle and we studied the evolution of their magnetic ordering and their low energy excitations (phonons and magnons) that could provide useful insights about their lattice and magnetic dynamics at the ground state.

The subsequent chapter 2 will introduce the main ingredients that characterize an spin-orbit insulator and the entangled pseudospin $J_{eff} = 1/2$ state. There, the magnetic excitation of the quasi-2D layered structure is described in terms of a Heisenberg model in the parent compound La_2CuO_4. In addition, theoretical studies stood that spin-lattice coupling leads to the stabilization of the magnetic ordering [6, 7]. Thus, the "pseudospin-lattice" coupling strongly depends on the strength of spin-orbit coupling and lattice degrees of freedom. We also describe the optical phonons that were previously analyzed with Raman scattering, and some anomalous results of high pressure studies where the system suffered phase transitions with competing magnetic orders.

Building upon the fact that the low energy excitations (phonons and magnons) provide useful insights about lattice and magnetic dynamics of the ground state, chapter 3 introduces the inelastic light scattering process (Raman scattering) which is an ideal and high resolution technique to study their low energy excitations. The strong spin-orbit coupling strength of the system is conducive to study their low lying energy coupling at their phonon, magnetic excitations and pseudospin-phonon coupling by its temperature dependence.

Chapter 4 shows the experimental procedure developed in this work and chapter 5 shows the response on its lattice, magnetic ordering, their optical phonons and a single magnon structure at the Brillouin zone center by X-ray diffraction, DC-Magnetization, and Raman scattering techniques. In chapter 6, we discuss the anomalous results by a possible influence at the entangled system $J_{eff} = 1/2$ that could be associated to a tetragonal instability and its magnetic configuration. Finally, in chapter 7 we conclude our work by summarizing the evidence that the "pseudospin-lattice" coupling strongly depends on many factors that need to be considered between the $J_{eff} = 1/2$ pseudospin and their lattice degrees of freedom.

Chapter 2

Sr_2IrO_4

The discovery of the Jeff = 1/2 Mott state on Sr_2IrO_4 (2008) [3] and the unique interplay of on-site Coulomb repulsion U, crystalline field and strong spin-orbit coupling of 5d-based materials have motivated an extensive investigation in this class of materials. In this chapter, we introduce the basis physics of the single layered iridate Sr_2IrO_4 and the importance of strong spin-orbit coupling that entangles locally the spin and orbital degrees of freedom. Additionally, intriguing consequences of pressure application in iridates is shown, where also their low energy excitations may own a clue to understand better their magnetic interactions on the ground state. For further information about iridates, there are many reviews on the literature about theoretical and experimental advances [1, 2, 4, 8].

2.1 Strong spin-orbit coupled Mott insulator Sr_2IrO_4

Among iridate material candidates, layered iridium oxides $Sr_{n+1}Ir_nO_{3n+1}$ of the Ruddlesden-Popper series have been an excellent playground to uncover novel physics. Its general structure consists of n Ir-O layers separated by 2 Sr-O layers along c axis. The most common phases investigated are with $n = 1$, 2 or infinite (perovskite structure). Each phase has Ir^{4+} ion centered on the octahedra IrO_6, where the crystal field splits its 5d atomic states into a triplet t_{2g} and a doublet e_g. The higher delocalized 5d orbitals open an energy gap about $10Deq \sim 3eV$ between the multiplets, which allows us to neglect the e_g orbital state for a low-spin d^5 electron configuration [9]. Thus, the ground state could also be considered as a single hole in the t_{2g} band. There, the t_{2g} manifold presents d-electrons in the $l_{eff} = 1$ effective state with orbitals $|l_z = 0\rangle \equiv |xy\rangle$, $|l_z = \pm 1\rangle \equiv -\frac{1}{\sqrt{2}}(i|xz\rangle \pm |yz\rangle)$. Furthermore, considering the strong spin-orbit coupling (SOC) of 5d band at Ir t_{2g} triplet, this splits into an effective total momentum $J_{eff} = 1/2$ doublet and $J_{eff} = 3/2$ quartet bands, resulting in a lower band $J_{eff} = 3/2$ being separated from the upper band $J_{eff} = 1/2$ by an energy of order $3\lambda/2$, where $\lambda \sim 0.4eV$ is the spin-orbit coupling strength [3]. As a result, the $J_{eff} = 3/2$ state is fully occupied and $J_{eff} = 1/2$ state is half filled.

It is known that 5d-ions produces a broader band in comparison to 3d systems, but in this case the strong SOC splits the t_{2g} band which produces a very narrow $J_{eff} = 1/2$ band. Thus, even a modest electronic correlation U compromised the Mott instability which is enhanced by the effective reduced bandwidth of $J_{eff} = 1/2$ doublet. In this way, a lower electronic correlation U and strong SOC cooperate to drive the system into an insulating state. This novel "spin-orbit assisted" Mott insulating state was proposed first on the work of Kim et al. [3] where a simple one band Hubbard model splits the $J_{eff} = 1/2$ band into a lower and upper Hubbard band with a small energy gap ~ 0.5 eV, resulting in a Mott insulator. Fig. 2.1 shows an scheme of the importance of strong orbit coupling SOC to be enhanced with a low electron correlation U to define this novel ground state.

X-ray absorption spectroscopy (XAS) measurements and first-principles band calculations at the same work stated that this novel ground state owns a coherent superposition of the three t_{2g} orbitals xy and xz/yz with opposite spin orientation [3]. Considering a perfect cubic symmetry ($\Delta = 0$), the ideal $J_{eff} = 1/2$ state could be represented as the following equation:

$$|J_{eff} = 1/2, \pm\rangle = \frac{1}{\sqrt{3}}(\pm|xy, \pm\rangle + |yz, \mp\rangle \pm i|xz, \mp\rangle), \tag{2.1}$$

which shows the entanglement of its orbit and spin degrees of freedom. Fig. 2.2 shows the real space representation of the pseudospin $J_{eff} = 1/2$ which brings also the importance of orbital and tridimensional characteristic that define a low magnetic moment differently to a spin S=1/2 only state.

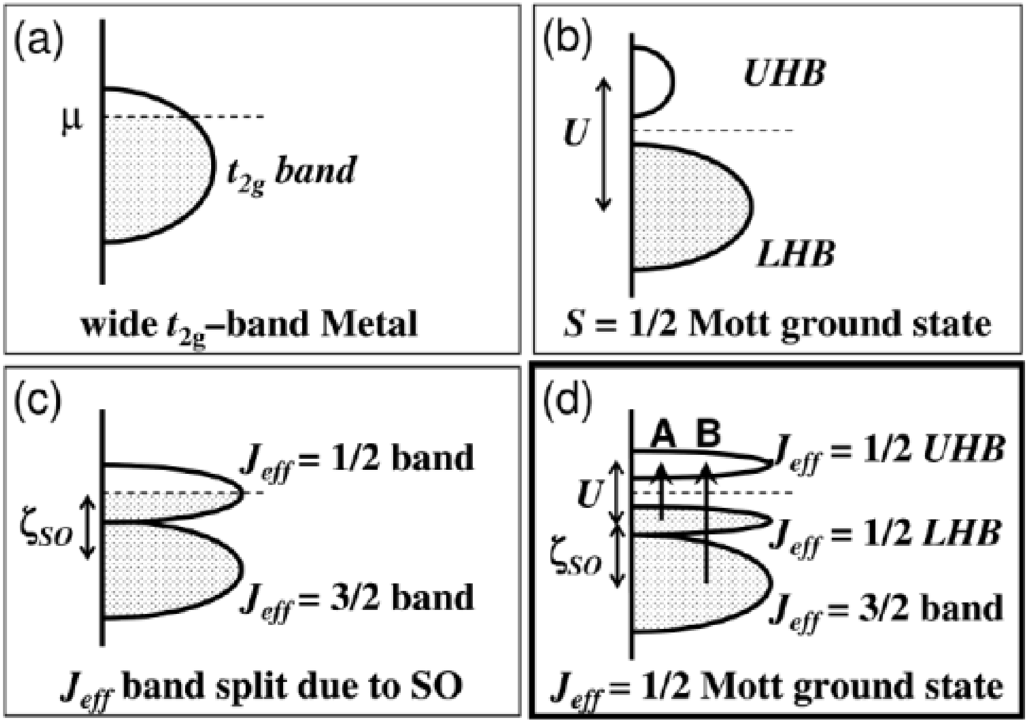

Figure 2.1: Schematic energy diagrams for the $5d^5$ configuration and interactions hierarchy for t_{2g} band: (a) without SOC and U representing a metal state; (b) with unrealistically large electron correlation U presents a S = 1/2 Mott state; (c) with a strong SOC, there is a split to a $J_{eff} = 1/2$ doublet and a $J_{eff} = 3/2$; and (d) with a strong SOC and low electron correlation U, the narrower $J_{eff} = 1/2$ doublet band splits with a small energy gap resulting a $J_{eff} = 1/2$ Mott state. The arrows depict possible optical transitions. *Figure adapted from* [3].

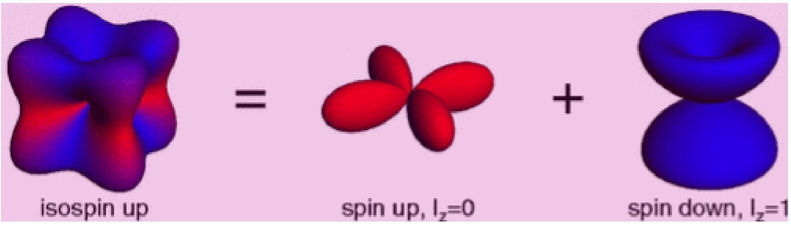

Figure 2.2: Isospin up real representation with a linear combination of $|xy, +\rangle$ with $l_z = 0$ and $(|yz, -\rangle + i|xz, -\rangle)$ with $l_z = 1$. *Figure adapted from* [6].

2.2 Structure and magnetic properties of the Quasi-2D single layer Iridate

This work focus on the study of Sr_2IrO_4, which belongs to the Ruddlesden–Popper iridates, $Sr_{n+1}Ir_nO_{3n+1}$ series with $n = 1$. It consists of a Quasi-2D single layer of IrO_2 sandwiched by two layers of SrO. Structural characteristics are a rotation of the octahedron IrO_6 around c-axis by $\alpha \sim 11°$, which enlarges its unit cell volume by a factor $\sqrt{2} \times \sqrt{2} \times 2$

compared to a higher symmetry of Sr_2RuO_4 ($I4/mmm$) and an elongation around the c axis by $\sim 5\%$. Then, this single layer iridate crystallizes in a tetragonal structure with a space group $I4_1/acd$ (No. 142) with a = b = 5.4846 Å and c = 25.804 Å at 13 K as shown in Fig. 2.3 [10, 11, 12].

More recent studies with neutron diffraction and second-harmonic generation (SHG) have revelead structural distorsions and forbidden reflections for the space group $I4_1/acd$ over a wide range of temperature, $4K < T < 600K$. It was also shown an absence of the c- and d- glide planes which indicated a lower symmetry that only a $I4_1/a$ (No. 88) space group could be suitable [12, 13, 14]. Furthermore, these lattice distortions arising from high temperature and the magnetic domains resulting in a unique in-plane axis moment orientation demostrated an orthorhombic symmetry in the resulting spin structure.

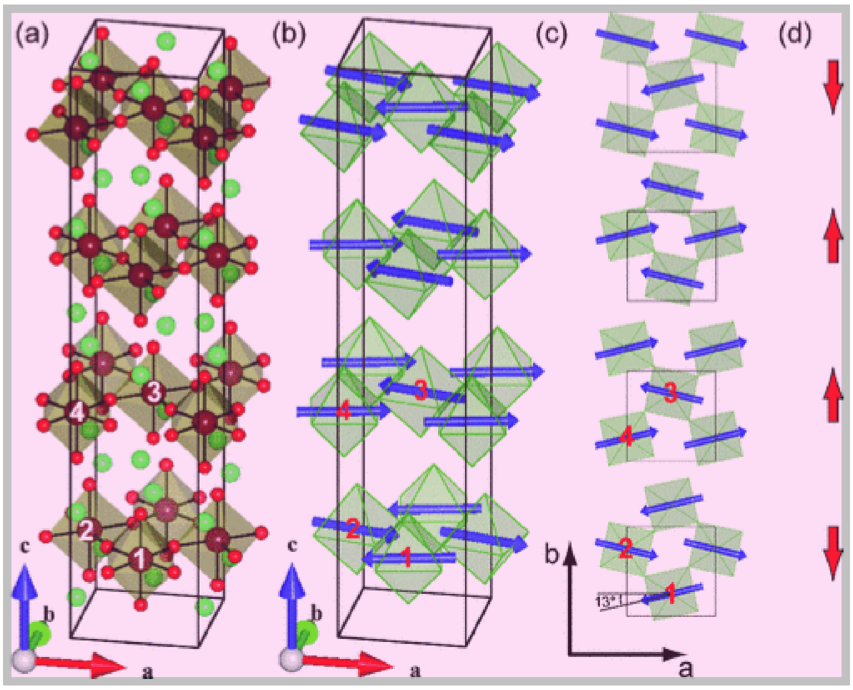

Figure 2.3: (a) The crystal structure of Sr_2IrO_4 with space group $I4_1/acd$. Each IrO_6 octahedron rotates 11.8° about the c axis and Ir atoms of the nonprimitive basis are labeled as 1, 2, 3 and 4. (b) The magnetic ordering of the $J_{eff} = 1/2$ state from single-crystal neutron diffraction measurements and (c) shows the same configuration in the basal plane. (d) The net canted moment projected along b axis for individual layers. Figure from Ref. [12]

Experimental magnetic studies have revealed that Sr_2IrO_4 has a canted AFM order with a transition temperature $T_N = 240$ K. This system has an ordered magnetic moment $\mu = 0.208(3)\mu_B$/Ir with a canted moment configuration within the basal plane. Its moment projections along a and b result in 0.202(3) and 0.049(2) μ_B/Ir respectively. Fig. 2.3 shows there is a net magnetic moment along b axis on a single layer where each has a staggered pattern ↓↑↑↓ along the c axis. The canting moment tilts by $\phi = 13°(1)$ from the a axis, which is similar to the IrO_6 octahedra rotation mentioned above. In addition, a theoretical study explained that there is a direct correlation between the lattice distortion and its magnetic ground state with non collinear magnetic moments, where the spin canting angle would rotate together with the IrO6 octahedra at the cubic limit of $J_{eff} = 1/2$ $(\phi/\alpha = 1)$ [6]. Also, it is suggested that an IrO_6 octahedra elongation (tetragonal distortion $\Delta > 0$) would lead to a decrease of the canting magnetic moment and give an upper estimate Δ marking a spin-flop transition to a collinear Antiferromagnetic order along the z-axis. Thus, there is indeed a direct correlation between the lattice distortion and its magnetic ground state.

2.2.1 Magnetic excitations

Many studies have initially interpreted that the ground state of the quasi-two dimensional square-lattice Sr_2IrO_4 are governed by isotropic Heisenberg interactions including anisotropic Dzyaloshinskii-Moriya (DM) interactions that cant the pseudospins and an interlayer coupling interactions that stabilize the stacking pattern "up-down-down-up" defined above the magnetic structure (sec. 2.2). However, there is evidence of a deviation from the Heisenberg universality class by a study of its critical magnetic properties suggesting an XY anisotropy character [15]. Moreover, a spin-wave gap which is a direct signal of the anisotropy was demonstrated by Raman scattering and RIXS experiments whose energy varies widely between ~ 1 meV and 30 meV [15, 16, 17, 18].

An extensive study by et. al. Kim [18] uses a set of techniques that showed the hierarchy among interactions which deviate from the Heisenberg universality class also that was reported earlier [15]. In that work, the possible mechanisms for an in-plane anisotropy were discussed applying a model coming from the interlayer interaction and from the coupling of the pseudospins to the lattice in addition to the isotropic Heisenberg model used by a theoretical basis [7]. These low energy pseudospin interactions could establish a Hamiltonian that uncovers the full three-dimensional static magnetic structure an the essential role of pseudospin-lattice coupling for square-lattice iridates.

These low energy interactions could be involved at the spin-wave dispersion Fig.

2.4 where it was identified as an out-of plane mode gaped at the Brillouin center zone [15]. The easy-plane anisotropy parameter determined was $\triangle_\lambda = 0.08(1)$, which was relatively larger than the observed for La_2CuO_4 [$\triangle_\lambda = 2.0(5) \times 10^{-4}$]. Indeed, that XY anisotropy was sufficiently strong to push the critical properties of Sr_2IrO_4 away from the isotropic 2D Heisenberg antiferromagnet model on a square lattice.

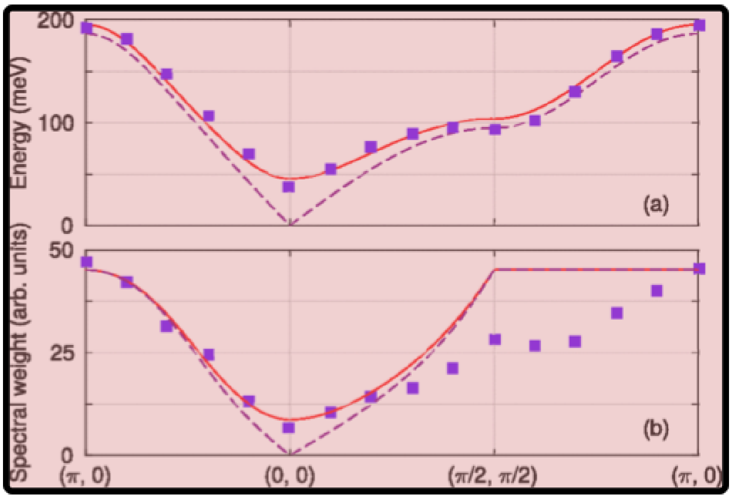

Figure 2.4: The solid and dashed lines were the best fit using the anisotropic 2D Heisenberg model [15]. The data in squares were obtained from fitting the single magnon peak in a RIXS experiment (ref. [19]). *Figure adapted from ref.* [15].

Moreover, inelastic neutron scattering and RIXS measured a magnon gap $\triangle_{\text{INS, RIXS}} \sim$ 2 meV at the magnetic zone center that was also consistent with calculated energies as well as the magnetic excitations identified by Raman scattering in previous studies [16, 17]. The in-plane magnon nature was probed by RIXS measured at Q = (3 2 28.2) using both polarization $(\pi - \sigma')$ and $(\pi - \pi')$ which probe only in-plane excitations.

Therefore, variations in magnetic interactions are reflected directly in its excitations. Entangled spin-orbit $J_{eff=1/2}$ state and relative crystal field interactions can induce this strong and unusual pseudospin-lattice interaction such as manganates. These anisotropic interactions might explain the resistance to have a transition to the superconductor or other competing states where experiments have also shown evidence of strong electron-phonon interactions on a metallic electron doped iridate with a short range magnetic order [16].

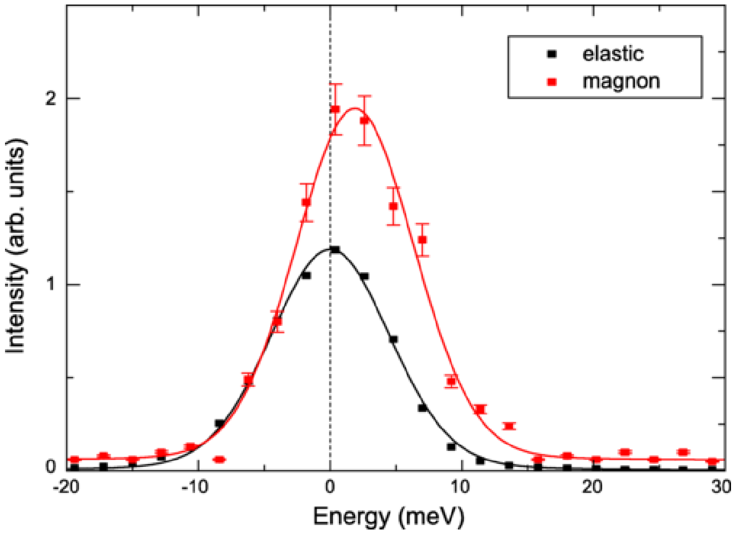

Figure 2.5: High-resolution RIXS intensity as a function of energy for incoherent scattering of Scotch tape used as a reference (black) and the in-plane magnon mode in Sr2IrO4 (red) measured at Q = (3 2 28.2) close to the magnetic zone center [18].

2.3 Tuning the system Sr_2IrO_4

The unique combination of strong spin-orbit coupling, intermediate on-site Coulomb interaction, and 5d extended orbitals have brought interest on possible new physics in iridates. For instance, the single layer and bilayer of the series $Sr_{n+1}Ir_nO_{3n+1}$ have both shown evidence of a charge gap and magnetic ordering transition with a weaker insulating behavior for $Sr_3Ir_2O_7$ ($n = 2$) [3, 20]. In contrast, bulk layered iridates with $n \geq 3$ are unstable under ambient pressure and the high pressure perovskite $SrIrO_3$ ($n = \infty$) presents a paramagnetic semi-metal state [20]. Thus, the proximity to this metal insulator transition for the single layer iridate and the similar magnetic exchange interactions from the system La_2CuO_4 with spin state S = 1/2 suggest the pseudospin state $J_{eff} = 1/2$ system with quasi 2D layer could host a possible superconductor state with electron doping or others competing orders [5].

In the context of strong relativistic SOC which entangles locally the spin and orbital degrees of freedom, sensitive signatures of anisotropic magnetic and structural properties were found via external parameters like temperature, pressure, and chemical doping. In addition, a pseudospin only Hamiltonian was insufficient for an accurate description of the magnetism of Sr_2IrO_4. Thus, the physics of such a system could differ from the cuprates, for which the SOC is only a weak perturbation and their nondegenerate orbitals e_g

exhibit also a weak coupling with the lattice [6]. Therefore, it was suggested the multiple pseudospins $J_{eff} = 1/2$, $J_{eff} = 3/2$ states and pseudospin-lattice coupling need to be considered for a realistic description of the layered iridates such as in the multiorbital manganates systems [7].

Besides the missing superconducting state, the nature of the low-energy interactions in iridates remains to be understood. Thus, the manipulation of the physical interactions via parameters such as pressure application, temperature dependence, or chemical doping could uncover their complex physics; meanwhile, the characterization of their lattice, charge, and magnetic degrees of freedom for the single layered Sr_2IrO_4 system could also allow us to understand better their low-energy interactions sensitive to anisotropic crystalline environments around the multi-spin/-orbital archetype $J_{eff} = 1/2$ state. For instance, a Raman scattering study of a single crystal Sr_2IrO_4 showed the existence of a strong anomalous isospin-phonon coupling effect below the magnetic ordering temperature (both own same meaning for the entangled state $J_{eff} = 1/2$ that is enhanced to a phonon), however, the mechanism of the microscopic exchange coupling remains unknown [21]. On the subject of applying pressure and temperature-dependent tuning studies, anomalous results were reported about their magnetic and electronic order discussing possible phase transitions within the tetragonal space group symmetry that could help to understand its unique physics [21, 22, 23, 24, 25, 26].

Therefore, we included below some previous studies of the system Sr_2IrO_4 which show anomalous properties and motivate us to apply the Raman scattering technique in order to detect the tuning effect of isovalent substitutions at the Sr site.

2.3.1 Sr_2IrO_4 under pressure

In order to tune the exchange interactions of the $J_{eff} = 1/2$, trying to mix the states $J_{eff} = 1/2$ and $J_{eff} = 3/2$, or modifying the canted antiferromagnetic order, there are many studies on the strong spin-orbit coupled system Sr_2IrO_4 under pressure, where it remained as an insulator to at least 40 GPa [24, 25, 26]. Indeed, it was shown a reduction of the resistance which means also a shortening of the insulating gap, but this avoided metallization remains unresolved and needs a better understanding. On the other hand, synchrotron techniques and Raman spectroscopy showed anomalous results which were understood hypothetically as magnetic transitions, anisotropic structural distortions and structural phase transitions [22, 23, 24, 25, 26]. Thus, it opened many scenarios of possible ordered or frustrated states.

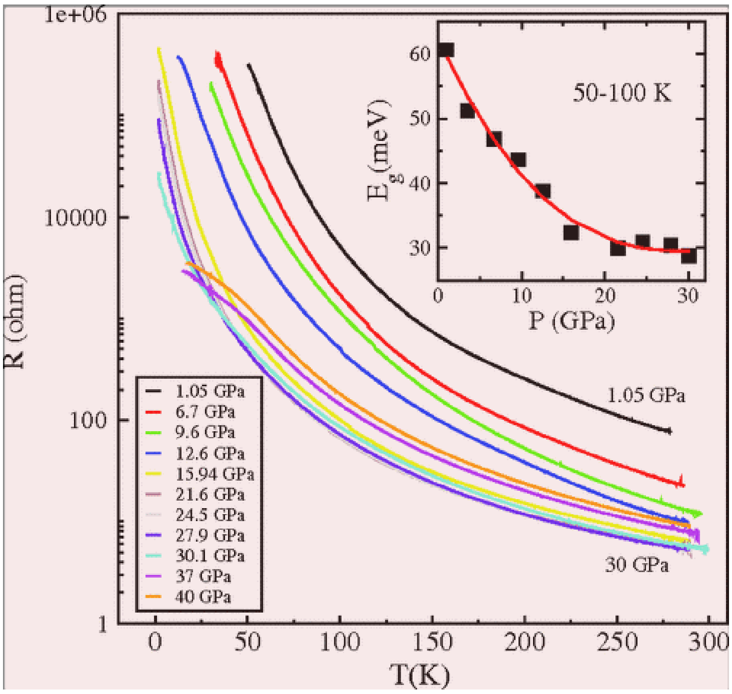

Figure 2.6: Temperature dependence of the resistance for Sr_2IrO_4 system under pressure (main panel). The inset figure shows an the insulating gap using $\ln(R) \propto E_g/2k_BT$ in the 50–100 K range. *Figure adapted from* [25]

In this context, our group reported a study focused on the evolution of structure, vibrational and compressibility properties of Sr_2IrO_4 under pressure [22, 23]. There, it was highlighted anomalous changes at 17, 30, and 40 GPa (see. fig. 2.7), where only above 40 GPa the system suffered a first order structural transition, and a phase coexistence of tetragonal and monoclinic states was observed over a wide pressure range. In addition, indications of anisotropic strain, anisotropic compressibility, and anomalous broadening at specific phonons were ascribed to phase transitions or crossovers of competing electronic states between 17 and 30 GPa within the tetragonal crystal symmetry.

Exploring the complexity of the $J_{eff} = 1/2$ system, an X-ray absorption spectroscopy study showed a significant sensitivity of the Ir t_{2g} orbitals above pressure and also a deviation from the strong spin-orbit cubic limit at ambient pressure [25]. There, the absorption branching ratio L_3/L_2 related to the <L.S> shows also an anomalous reduction at ~ 30–40 GPa describing a clear mixing $J_{eff} = 1/2$ and $J_{eff} = 3/2$ states, whereas there is an increased tetragonal crystal field. Additionally, it is observed a sharp magnetic phase

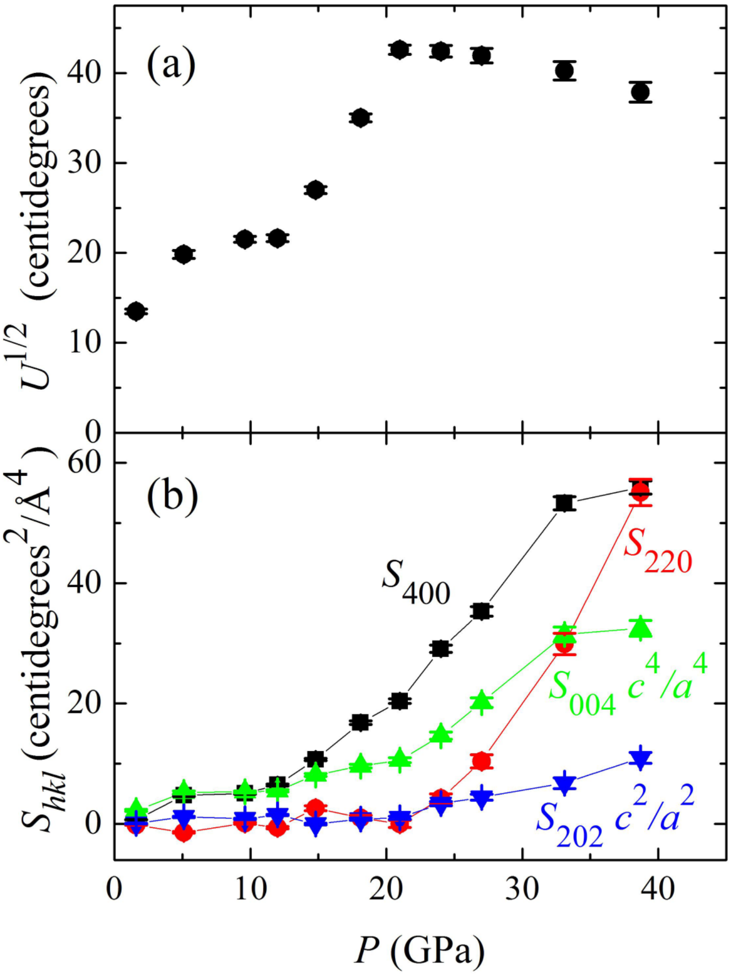

Figure 2.7: Isotropic Gaussian (a) and anisotropic Lorentzian (b) strain broadening parameters of Bragg peaks after the refinement process of the ground system under pressure. *Figure adapted from* [22].

transition at 17 GPa, where the canted Antiferromagnetic order is sensible to the XMCD (X-ray magnetic circular dichroism) measurement, however, it suddenly vanished at the same applied pressure that our group also pointed anomalous results for structural and vibrational properties (17 GPa).

Using X-ray resonant magnetic scattering technique to determine its magnetic structure above pressure, another study by Haskel *et. al.* showed a crossover of magnetic structures around 7 GPa mimicking the effect of an applied magnetic field at ambient pressure [26]. Moreover, the system suffered an order-disorder magnetic phase transition with no long range order detected above 17–20 GPa. In this way, they also performed an XMCD applying a field up to H = 6 T trying to induce a magnetic order, however, the temperature dependence of lower XMCD intensity was a signal of a persistance exchange interaction owning a highly frustrated magnetic state. In light of these studies, they suggested different possible scenarios of realization of novel quantum paramagnetic phases, charge density wave or other emergent states below 40 GPa, even considering that the system still keep an entangled pseudospin state $J_{eff} = 1/2$. These results opened exciting questions about the nature of their magnetic interactions in iridates, which may lead to further insight about the avoid of metallization and the missing superconductivity in electron-doped iridates.

2.3.2 Sr_2IrO_4 Raman active modes

It is important to mention that in this section it is only shown 4 specific detected Raman structures, because our work is also based on these same Raman structures [22]. The *ab-initio* lattice dynamics calculations have identified these Raman active phonon modes where fig. 2.9 exhibits their mechanical representations [22]. The pressure application and temperature dependence for these low energy excitations showed anomalous behavior too which need further investigation [21, 22].

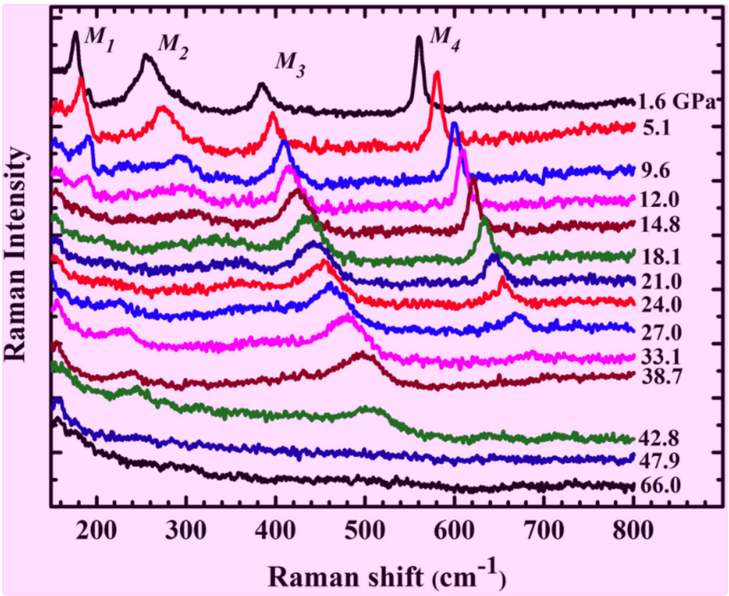

Figure 2.8: Raman spectra of Sr_2IrO_4 at room temperature at several pressures. The phonon peaks associated with modes M_1 and M_2–M_4 are represented in Figs. 2.9 (a)–(e). *Figure and caption adapted from ref.* [22].

At fig. 2.8, it is shown four peaks that dominates the spectrum at 180, 260, 390, and 560 cm^{-1} labeled as M_1-M_4 at P= 1.6 GPa and room temperature. *Ab-initio* calculations identified accurately these modes. There, peak M_1 is indeed a superposition of an A_{1g} symmetry mode which represents a rotation of the IrO_6 along the *c*-axis combined with an in-phase Sr displacement along c, and a B_{2g} symmetry mode is an out-of-phase Sr vibration. Peak M_2 has A_{1g} symmetry and represents a pure rotational mode (or, more accurately librational mode) of the IrO_6 octahedra along c. Peak M_3 has B_{2g} symmetry and is an in-plane bending mode of the O-Ir-O at its base plane. Peak M_4 has A_{1g} symmetry and is a stretching mode involving a Ir-O(apical) modulation.

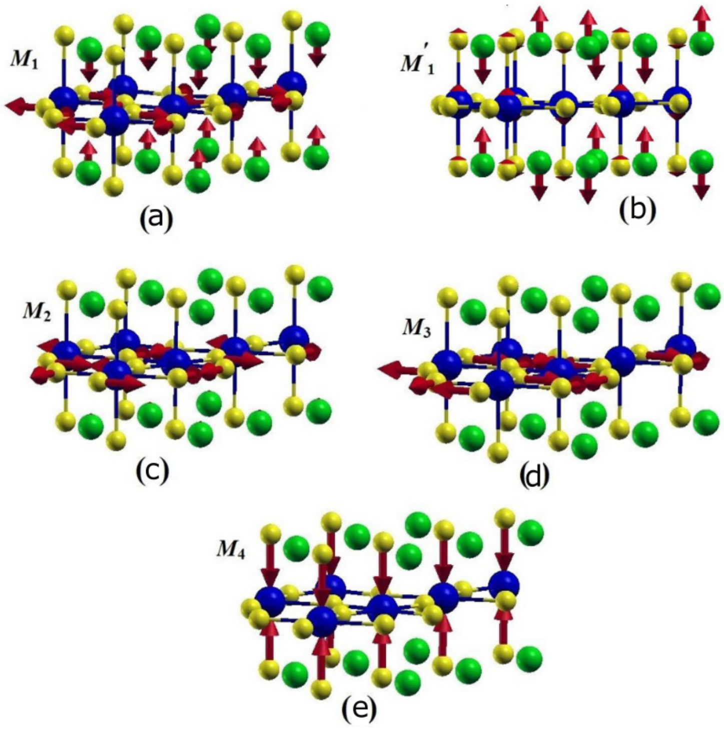

Figure 2.9: (a)–(e) Mechanical representations of modes M_1/M'_1 ($\sim$ 185 cm^{-1}), M_2 ($\sim$ 270 cm^{-1}), M_3 ($\sim$ 395 cm^{-1}), and M_4 ($\sim$ 570 cm^{-1}). Spheres blue, green and yellow represent Ir, Sr and O atoms, respectively. *Figure is adapted from ref.* [22].

The work related to the Raman scattering of Sr_2IrO_4 under pressure reveled phonon anomalies below 40 GPa suggesting competing electronic ground states at the tetragonal phase [22]. Fig.2.10 shows the frequencies, linewidths of the M_1-M_4 phonon modes and its pressure dependence. It was interesting to note that they present anomalies at 17 , 30 and 40 GPa. The broadening linewidths from modes M_3 and M_4 resembled the pressure dependence of the S_{400} Lorentzian strain broadening parameter (fig. 2.7). In addition, Mode M_3 shows an asymmetric profile between 17 and 40 GPa fitted with a Fano line shape which implies an electronic continuum coupled to this lattice vibration mode [27].

The temperature dependence of the same phonon modes also owns an interesting behavior [21]. It is known that phonons may be sensitive to the exchange interaction $H = -\sum J_{ij}\langle S_i.S_j\rangle$, where the exchange integral J_{ij} is a function of the ions position

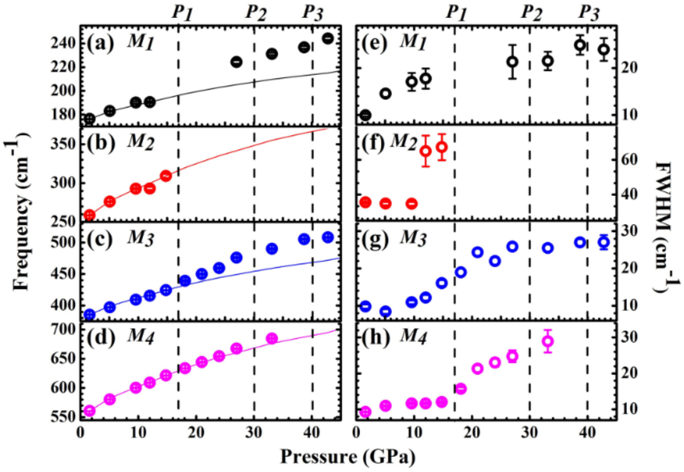

Figure 2.10: (a)–(d) Pressure dependence of frequency modes M_1–M_4, and (e)–(h) are respectively the full width at half-maximum (FWHM) of the Raman peaks. The phonon anomalies are marked with vertical dashed lines at pressures P_1 = 17 GPa, P_2 = 30 GPa, and P_3 = 40 GPa. The solid lines in (a)–(d) represent scalings according to the Grüneisen's law. *Figure and caption adapted from ref.* [22].

that participate on the integral path between ions i and j. There, the Taylor expansion of the exchange integral gives a dynamical term responsible to a spin-phonon coupling. Afterwards, it was observed an anomalous hardening bellow the transition temperature T_N which is a manifestation of the pseudospin-phonon coupling (fig. 2.11) even considering the anharmonicity of its phonon-phonon interaction.

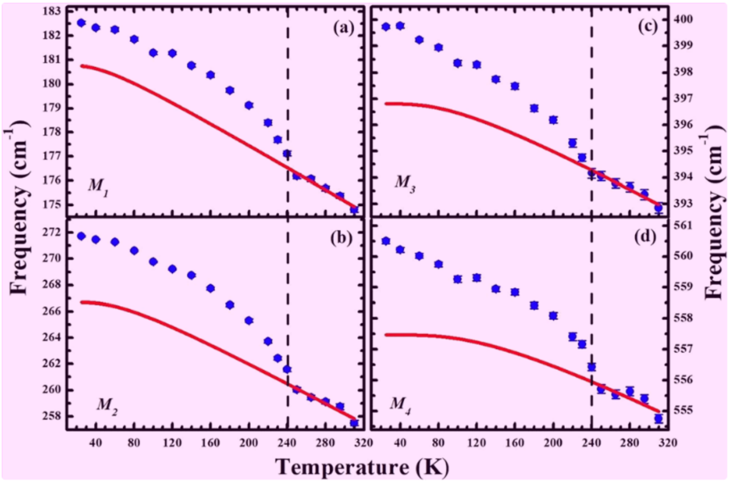

Figure 2.11: (a)–(d) Temperature dependence of the phonon modes M_1-M_4 represented by solid circles. The solid lines represents the anharmonic behavior from the two-phonon decay process. *Figure adapted from ref.* [21].

Chapter 3

Raman Spectroscopy

Raman spectroscopy is a standard tool for the material characterization, applied also to a wide variety of materials science problems. Historically, it was associated with the scattering of light by optical phonons in solids and molecular vibrations, however, it could refer to inelastic scattering by any low energy excitations associated to the degrees of freedom from ions and electrons in crystalline or amorphous solids. In this chapter, it is introduced the basics physics involved on the first order inelastic scattering by lattice vibrations and approximations besides the harmonic model. For further theoretical and experimental treatments there are referenced books by Hayes and Loudon [28] and the series Light Scattering in Solids [29, 30, 31].

3.1 Inelastic scattering of Light

The inelastic light-scattering let us determine the energy excitations by measurement of frequency shift ω from a monochromatic incident light ω_I with polarization e_I. The contribution comes from an energy gain ω_S (Stokes component) or an energy losses ω_{AS} corresponding to various excited states of the sample. Fig. 3.1 shows a Raman espectra from CCl_4 sample using a monochromatic excitation $\lambda = 488.0nm$. The central peak represents the elastic component (Rayleigh scattering) with the same frequency of the incident light. Then, normally the resulting Stokes and Antistokes components remain similar shift ω from the central peak. Stokes' components are negative from an absorption or creation of a phonon excitation, and Antistokes' component are positive from an emission or destruction of phonon excitation as it is showed at the fig. 3.1. These intensities are related by

$$n(\omega)\frac{d^2\sigma}{d\Omega d\omega_S} = (n(\omega)+1)\frac{d^2\sigma}{d\Omega d\omega_{AS}}, \tag{3.1}$$

where $n(\omega) = \frac{1}{\exp(\hbar\omega/\mathrm{k}_B\mathrm{T})-1}$ is the Bose-Einstein thermal factor, k_B is Boltzmann's constant, T is the sample's temperature, and $\frac{d^2\sigma}{d\Omega d\omega_{S,AS}}$ is the spectral differential cross section measured for a fixed scattering angle for Stokes or Antistokes' component of the spectrum.

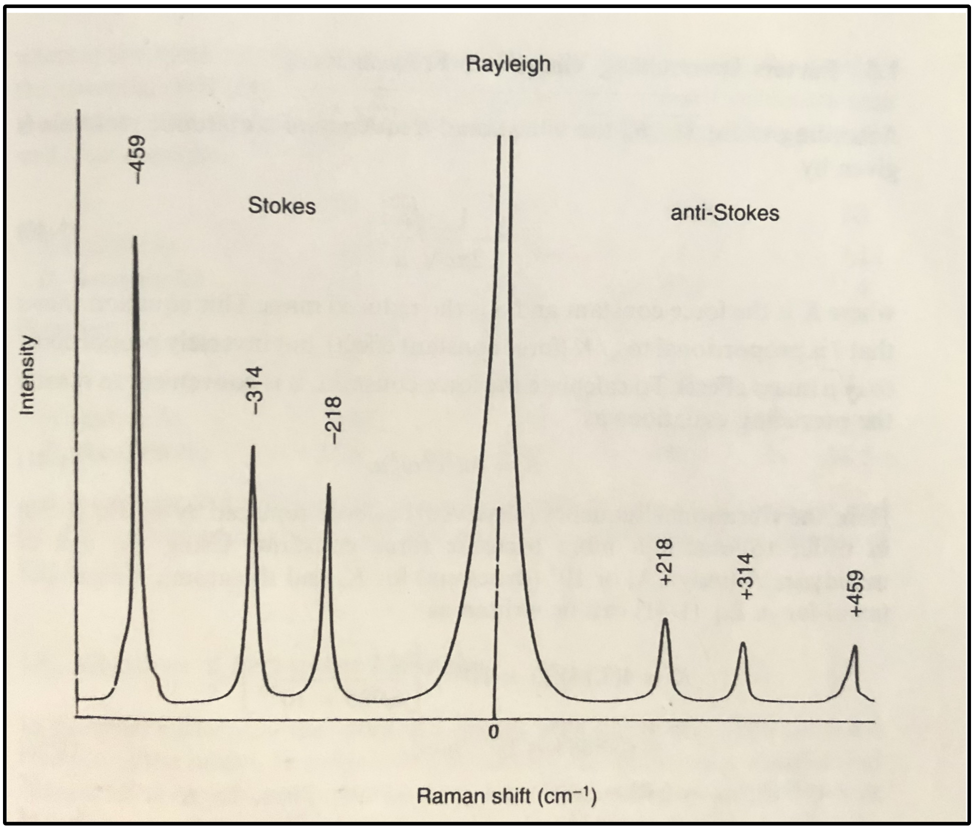

Figure 3.1: Raman spectra of CCl_4 using a monochromatic incident excitation. *Figure adapted from ref.* [32].

Inelastic light-scattering process owns properties of energy and momentum conservation for crystals. Thus, Stokes component indicates a sample gains $\hbar\omega$ energy, where $\omega = \omega_I - \omega_S$ and also gains a momentum $\hbar\mathbf{q}$, where $\mathbf{q} = \mathbf{k_I} - \mathbf{k_S}$. In contrast, the Antistokes component indicates the sample loses $\hbar\omega$ energy, where $\omega = \omega_{AS} - \omega_I$ and also loses a momentum $\hbar\mathbf{q}$, where $\mathbf{q} = \mathbf{k_{AS}} - \mathbf{k_I}$.

The Raman scattering experiments are usually performed with a laser in the visible regime, where its frequency is on the order of $\sim 5\times10^{15}$Hz. Meanwhile, studied excitations are usually in the range [3x10^{11}, 10^{14}Hz], which are equivalent to excitations between 10 and 3000 cm^{-1}, so most experiments satisfy $\omega \ll \omega_I$. Thus, the wavevector magnitude for low energy crystal excitations is $q = 2k_I \sin\frac{\phi}{2}$, where typically the maximum wavevector at a backscattering geometry is about $10^7\mathrm{m}^{-1}$ and Brillouin lattice is about $3 \times 10^{10}\mathrm{m}^{-1}$.

3.1.1 Macroscopic approach of Inelastic Light Scattering

Inelastic light scattering, using the classical harmonic oscillator theory, can be treated by two approaches: the microscopic and macroscopic method. The first approach treats the atom quantum mechanically. Scattering by lattice vibrations (phonon) or spin waves (magnon) involves the interaction Hamiltonian in terms of electric-dipole operator or using the matrix elements of the spin operator between atomic wavefunctions, respectively. Thus, the microscopic approach could provide a deeper understanding of the nature of the light scattering process. On the other hand, macroscopic method applies directly with the macroscopic variables such as the polarization vector with usual Maxwell equations.

The macroscopic approach of inelastic light scattering is applied on an extended medium, where the electric component of the incident light induces a macroscopic polarization vector $\mathbf{P}(\mathbf{r}, t)$ in the sample, which in the absence of any excitations is

$$\mathbf{P}(\mathbf{r}, t) = \epsilon_0 \chi(\omega_I) \mathbf{E}_I(\mathbf{r}, t), \tag{3.2}$$

where $\chi(\omega_I)$ is a tensor called the linear or first-order susceptibility of the medium. Indeed, excitations are capable to modulate this quantity linearly in terms of $X(\mathbf{r}, t)$ which could represent a vibrational displacement or a deviation of the magnetization in a magnetic crystal. Thus, considering only a second order susceptibility χ', the equation for the polarization vector is replaced by

$$\mathbf{P}(\mathbf{r}, t) = \epsilon_0 (\chi \mathbf{E}_I + \chi' X \mathbf{E}_I), \tag{3.3}$$

The first term of this equation is responsible for the elastic scattering. In contrast, the second term oscillates at different frequency because $X(q, \omega)$ is itself time-dependet function and this second order polarization vector is responsible for the inelastic contribution of the light scattering with $\omega_S = \omega_I - \omega$ (Stokes component) and $\omega_{AS} = \omega_I + \omega$ (Antistokes component). Then, the expressions of polarization with X, and E_I in the Fourier representations leads on these time dependence expressions

$$\mathrm{P}^i_S(\mathbf{K}_S, \omega_S) = \epsilon_0 \chi^{ij}(\omega_I, -\omega) X^*(\mathbf{q}, \omega) \mathrm{E}^j_I \tag{3.4}$$

$$\mathrm{P}^i_{AS}(\mathbf{K}_{AS}, \omega_{AS}) = \epsilon_0 \chi^{ij}(\omega_I, \omega) X(\mathbf{q}, \omega) \mathrm{E}^j_I. \tag{3.5}$$

The second order susceptibility χ' is a matrix χ^{ij}, which expresses the change of its susceptibility caused by an excitation X, expressed as $\chi^{ij}(\omega_I, -\omega) = \partial\chi^{ij}(\omega_I)/\partial X^*_q$, where the excitation frequency is usually much smaller than the incident light and it is often a good approximation to set ω to zero. Thus, the second order susceptibility would be caused by a *static* excitation amplitude $X(q, 0)$.

Cross Section

The total scattering cross section σ is a result of the collected light scattering process in all the directions by different excitations. It provides a measure of the intensity, although it is difficult to collect experimentally in all directions. However, it could be detected over a typical solid angle Ω with the detector on a fixed position. In addition, experiments also focus on the scattering process by a specific excitation with a particular frequency ω. Thus, the scattering light intensity detected for a specific excitation at a particular position is named the spectral differential cross section, $d^2\sigma/d\Omega d\omega_S$, which has a general expression as

$$\frac{d^2\sigma}{d\Omega d\omega_S} = \frac{\omega_I \omega_S^3 \upsilon V \eta_S \langle \varepsilon_S \cdot \mathbf{P}^*_S(\mathbf{k}_S) \varepsilon_S \cdot \mathbf{P}_S(\mathbf{k}_S) \rangle_{\omega_S}}{(4\pi\epsilon_0)^2 c^4 \eta_I |E_I|^2}, \tag{3.6}$$

for a Stokes process, where υ us the volume of the sample that contribute to the light scattering detected, V is the sample volume which is cancelled with a factor $1/V$ that comes from the power spectrum as a normalization volume and η_S/η_I is the refractive index ratio. In addition, there is the frequency factor $\omega_I \omega_S^3$ and the power spectrum of the polarization fluctuations which both determine the strength and profile shape of the scattered spectrum. The power spectrum of the polarization could also be written using the excitation amplitudes as,

$$\langle \varepsilon_S \cdot \mathbf{P}_S^*(\mathbf{k}_S) \varepsilon_S \cdot \mathbf{P}_S(\mathbf{k}_S) \rangle_{\omega_S} = |\epsilon_0 \varepsilon_S^i \varepsilon_I^j \chi^{ij}(\omega_I, -\omega) E_I^j|^2 \langle X(\mathbf{q}) X^*(\mathbf{q}) \rangle_\omega, \tag{3.7}$$

, where repeated indices represents a summation as a convention, and $\varepsilon_I, \varepsilon_S$ are unit vectors parallel to the incident and scattered field, respectively. Thus, the power spectrum depends on the fluctuation properties of the scattering excitation.

The fluctuation properties of a scattering excitation could be accounted for by using the general fluctuation-dissipation theory found in chapter 12 of Landau and Lifshitz [33]. Here, we briefly show a simple classical case using the fluctuation properties of a vibrational excitation considering a displacement motion W_σ represented by a harmonic oscillator equation

$$\ddot{W}_\sigma + \Gamma_\sigma \dot{W}_\sigma + \omega_\sigma^2 W_\sigma = 0 \tag{3.8}$$

where ω_σ is its natural frequency, Γ_σ is its damping constant, and σ label a mode of vibration. Then, it is inserted a fictitious driving force $F(t)$ that couples to excitation ω_σ. As the time dependence is arbitrary, it is Fourier analyzed. Thus, we have the following harmonic equation on its Fourier transformation form

$$(\omega_\sigma^2 - \omega^2 - i\omega\Gamma_\sigma) W_\sigma(\mathrm{q}, \omega) = F(\omega), \tag{3.9}$$

where the amplitude excitation Fourier component $W_\sigma(\mathrm{q}, \omega)$ is proportional to the force, written as

$$W_\sigma(\mathrm{q}, \omega) = T(\mathbf{q}, \omega) F(\omega) \tag{3.10}$$

The fluctuation dissipation theory stands that the power spectrum is as follows,

$$\frac{1}{2} \langle X * (\mathbf{q}) X(\mathbf{q}) + X(\mathbf{q}) X * (\mathbf{q}) \rangle_\omega = \frac{\hbar}{\pi} \{ n_\omega + \frac{1}{2} \} Im T(\mathbf{q}, \omega) \tag{3.11}$$

.

Thus, using eqs. 3.9 and 3.10, we obtain the following expression

$$\mathrm{Im}T(\mathbf{q},\omega) = \frac{\omega\Gamma_\sigma}{N\{(\omega_\sigma^2-\omega^2)^2+\omega^2\Gamma_\sigma^2\}} \approx \frac{\pi g_\sigma(\omega)}{2N\omega_\sigma} \tag{3.12}$$

Molecular vibrations usually have Γ_σ much smaller than ω_σ. Then, we could approximate the profile lineshape to a Lorentzian dependence with a $g_\sigma(\omega)$ function, where

$$g_\sigma(\omega) = \frac{\Gamma_\sigma/2\pi}{(\omega_\sigma-\omega)^2+(\Gamma_\sigma/2)^2} \tag{3.13}$$

The resulting cross section for Stokes scattering by using the relations 3.6 and 3.13 is

$$\frac{d^2\sigma}{d\Omega d\omega_S} = \frac{\hbar\omega_I\omega_S^3\upsilon V\eta_S|\epsilon_0\varepsilon_S^i\varepsilon_I^j\chi^{ij}(\omega_I,-\omega_\sigma)|^2\{n(\omega_\sigma)+1\}}{(4\pi\epsilon_0)^2 2c^4\eta_I N\omega_\sigma} g_\sigma(\omega), \tag{3.14}$$

3.2 Lattice dynamics

Theoretical derivation of the crystal lattices properties is out of the scope of our study. This section brings an outline in order to understand some of our results . Accounts to reach the dynamical properties of crystal lattices can be found in many reference books [34, 35, 36]. The theory to describe the crystal-lattice vibrations and its frequencies uses the harmonic approximation. This theory relies on two assumptions: each ion oscillation is associated to a mean position $\mathbf{R}$ and not a fixed position, and the typical oscillation $u(\mathbf{R})$ from its equilibrium position is small compared to the interionic spacing [37]. Thus, the harmonic approximation expands the total potential energy of the crystal to a second order:

$$U^{\mathrm{harm}} = \frac{1}{2}\sum\sum\Phi_{\alpha\beta}u_\alpha u_\beta, \tag{3.15}$$

where u_α is the α atom's displacement from its equilibrium position, and $\Phi_{\alpha\beta}$ is the harmonic force constant. Thus, the motion of an α atom having a mass M_α is

$$M_\alpha\ddot{u}_\alpha = \sum_\beta \Phi_{\alpha\beta}u_\beta. \tag{3.16}$$

The equations of motion is a linear combinations of $3n$ equations considering the motion of n atoms. It is formally solved by further transformations which decouples into 3n noninteracting collective oscillations called normal modes. The transformations coefficients satisfy orthonormality relations and transform the atomic displacement to the normal coordinates W_σ, where $\sigma(= 1, 2, ..., 3n)$ is a branch index. Resulting in collective oscillations with an equation of the form:

$$\ddot{W}_\sigma + \omega_\sigma^2 W_\sigma = 0 \tag{3.17}$$

where, ω_σ is the natural vibrational frequency.

3.2.1 Anharmonic interactions

Many physical phenomena need to consider further corrections to the harmonic approximation. For instance, when there is enough thermal energy, it is important to consider the phonon-phonon interaction. Experimentally it is observed on the Raman spectra where its frequencies are diminished and linewidths are incremented.

Theoretical and experimental works about anharmonic decay of optical phonons have established that the principal process results on the phonon decay into two acoustic phonons of opposite momentum keeping the momentum conservation on the light scattering by the crystal [38, 39, 40]. In addition, Balkanski included an extension including a four-phonon process for the frequency shift and damping constants for higher temperature range [38]. Thus, anharmonic properties could came out from both cubic and quartic order of the crystal potential. These terms are included to the vibrational Hamiltonian as

$$\begin{aligned} H =& \frac{1}{2}\sum \frac{1}{M_\alpha} P^2 + \frac{1}{2}\sum\sum \Phi_{\alpha\beta} u_\alpha u_\beta \\ &+ \frac{1}{6}\sum\sum\sum \Phi_{\alpha\beta\gamma} u_\alpha u_\beta u_\gamma + \frac{1}{24}\sum\sum\sum\sum \Phi_{\alpha\beta\gamma\delta} u_\alpha u_\beta u_\gamma u_\delta, \end{aligned} \tag{3.18}$$

where u_α is the α atom's displacement from its equilibrium position, and $\Phi_{\alpha\beta}$, $\Phi_{\alpha\beta\gamma}$, and $\Phi_{\alpha\beta\gamma\delta}$ are the second order harmonic, cubic anharmonic and quartic anharmonic force constants, respectively. These anharmonic terms can be can be diagrammatically represented on fig. 3.2 at the scattering process. For instance, fig. 3.2 (a), (b) can be viewed as a process involving the absorption of an incident photon $\hbar\omega_I$, emission of a scattered photon $\hbar\omega_S$, and a creation of an optical phonon ω_0 that decays anharmonically into two or three phonons that arise from the cubic and quartic order of the anharmonic Hamiltonian. Then, Balkanski applied Klemens' model [40] associating the frequency shift $\triangle(T)$ and the damping constant $\Gamma(T)$ to three and four phonon process. Thus, he came up with the following equations [38]

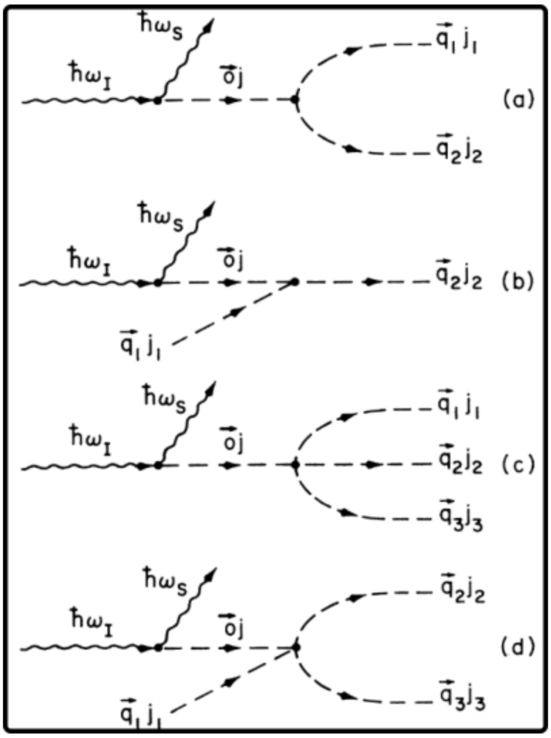

Figure 3.2: Diagrams representing the decay of a Raman active phonon mode into two phonons (a) and three phonons (c). However, the decay process can also occur by an absorption of another phonon and the emission of one (b) or two phonons (d). *Figure adapted from ref.* [38].

$$\begin{aligned} \omega(T) =& \omega_0 + \triangle(T) \\ \triangle(T) =& A\left[1 + \frac{2}{\exp^x - 1}\right] + B\left[1 + \frac{3}{\exp^y - 1} + \frac{3}{(\exp^y - 1)^2}\right] \\ \Gamma(T) =& C\left[1 + \frac{2}{\exp^x - 1}\right] + D\left[1 + \frac{3}{\exp^y - 1} + \frac{3}{(\exp^y - 1)^2}\right] \end{aligned} \tag{3.19}$$

where $x = \hbar\omega_0/2k_BT$ and $y = \hbar\omega_0/3k_BT$ are simple factors which satisfy the energy conservation. There, ω_0 is emitted two phonons with $\omega = \omega_0/2$ at the cubic anharmonic decay and/or ω_0 emitted three phonons with $\omega = \omega_0/3$ at the quartic anharmonic decay within the constraint of moment conservation. Thus, the temperature behavior of $\triangle$ and

Γ vary linearly with T for the cubic anharmonic multiplying factors A, C constants at temperatures higher than the Debye temperature; and the quartic anharmonic terms multiplying B, D constants vary quadraticaly with T. However it should be expected that contribution of four phonon process would be small compared to the three phonon process.

Anharmonic interactions representing three and four phonon process could have more channels contributing with the Raman active phonon mode associated with other diagrams as fig. 3.2 (c)(d), however, the rate of decay would just introduce terms also varying linearly to T or T^2 at higher temperatures.

3.2.2 Spin-Phonon coupling

Magnetic insulating materials are reasonably explained by the theory of superexchange interaction, where there is an indirect interaction mediation by non-magnetic ions which are placed between the magnetic ions. Thus, there would be an spin-phonon coupling when the optical phonon is involved to the relative displacement of the non-magnetic ions that also cooperate on the super-exchange interaction between magnetic ions. In consequence, when the second derivative of the exchange interaction is large enough there could be an effect on the optical phonon frequency that could be sensitive by Raman scattering at the magnetic long state order (T < T$_C$).

Baltensberger has explained this effect on the optical phonon using the model of Heisenberg for an Europium Oxide structure [41], where the spin energy is determined by

$$H_S = -\sum_{i,j>i} J_{i,j} \langle S_i \cdot S_j \rangle, \tag{3.20}$$

where $J_{i,j}$ is the superexchange coupling function of the magnetic ions arrange i, j and the intermediate non-magnetic ions, $\langle S_i \cdot S_j \rangle$ is the correlation function of the spin operators. Thus, the variation of exchange function associated to the σ optical phonon until its second order Taylor expansion is described as,

$$\triangle J^{\sigma}_{i,j} = [\mathbf{u}^{\sigma}_k \cdot \nabla_k] J_{i,j} + \frac{1}{2}[\mathbf{u}^{\sigma}_k \cdot \nabla_k]^2 J_{i,j} \tag{3.21}$$

where $\mathbf{u}^{\sigma}_k$ is a displacement vector from the kth non magnetic ion placed between the i, j magnetic ions and associated to the σ phonon mode. The linear first term from eq. 3.21

has null contribution to the average exchange, however, the second order might have a contribution to the phonon frequency, which is responsible to the spin-phonon coupling [42, 43]. Indeed, we could generalize the variation of the exchange energy due to all the lattice vibrations including eq. 3.21 into the spin energy hamiltonian as:

$$\begin{aligned}\Delta H^{s-l} &= -\frac{1}{2}\sum_{i,j>i}\sum_{k}[\mathbf{u}_k^\sigma \cdot \nabla_k]^2 J_{i,j}\langle S_i \cdot S_j\rangle \\ &= -\frac{1}{2}\left(\sum_{k}[\mathbf{u}_k^\sigma \cdot \nabla_k]^2\right)\left(\sum_{i,j>i} J_{i,j}\langle S_i \cdot S_j\rangle\right)\end{aligned} \tag{3.22}$$

The ∇_k operator from this equation is related to the displacement of k independently of the correlation function $\langle S_i \cdot S_j\rangle$, so the second order expansion of the spin energy could also be expressed as:

$$\begin{aligned}\Delta H^{s-l} &= -\frac{1}{2}\sum_{k}[\mathbf{u}_k^\sigma \cdot \nabla_k][\sum_{i,j>i}(\nabla_k J_{i,j})\langle S_i \cdot S_j\rangle \cdot \mathbf{u}_k^\sigma] \\ &=\frac{1}{2}\sum_{k}\mathbf{u}_k^\sigma \cdot \left[-\sum_{i,j>i}(\nabla_k^2 J_{i,j})\langle S_i \cdot S_j\rangle\right] \cdot \mathbf{u}_k^\sigma\end{aligned} \tag{3.23}$$

We also need to describe the potential energy of the lattice where within the harmonic approximation and it could be expressed as:

$$U^{lattice} = \frac{1}{2}\sum_{k,k'}\mathbf{u}_k^\sigma \mathbf{D}_{k,k'}^{lattice}\mathbf{u}_{k'}^\sigma \tag{3.24}$$

which is a form used on the chap. 22 of Ashcroft and Mermin (1976)

$$\begin{aligned}\mathbf{D}_{k,k'}^{lattice} &= \delta_{k,k'}\sum_{k'}\Phi_{k,k'} + \Phi_{k,k'} \\ (\Phi_{k,k'})_{l,m} &= \frac{\partial^2 \phi_{k,k'}}{\partial r_{k,k'}^l \partial r_{k,k'}^m}\end{aligned} \tag{3.25}$$

where $\phi_{k,k'}$ is the force constant between ion k an k'; and $r_{k,k'}^l$ is the l component of the relative position vector. Thus, the variation of a magnetic exchange expressed above could be add to the potential energy as:

$$U = U^{lattice} + \Delta H^{s-l} = \frac{1}{2}\sum_{k}\mathbf{u}_k^\sigma\left(\mathbf{D}_{k,k}^{lattice} + \mathbf{D}_k^{spin-phonon}\right)\mathbf{u}_k^\sigma + \frac{1}{2}\sum_{k,k'\neq k}\mathbf{u}_k^\sigma \mathbf{D}_{k,k'}^{lattice}\mathbf{u}_k^\sigma \tag{3.26}$$

At simple qualitatively analyzing, if ΔH^{s-l} is negative, the spin-phonon coupling could contribute to the magnetic order stability at $T < T_C$ and also reducing the potential energy of the crystal that as a consequence the involved phonons could also reduce its energy.

Chapter 4

Experimental Method

In this chapter, we are going to introduce the experimental method developed on this dissertation. At the beginning we proceed with the samples synthesis, then we characterize qualitatively and quantitatively the structural and magnetic behavior of the samples. Finally, we measure its Raman scattering.

4.1 Sample Synthesis

The synthesis of our samples were done using the solid state reaction, which their powder reactants are mixed together and then heated in a furnace. The principle mechanism to achieve good quality of polycrystalline samples is linked to have a sufficient kinetic energy to satisfy solid state counter-diffusion of ions between different particles to bring together atoms in the correct stoichiometric ratio [44].

The single layer iridate with chemical substitutions at Sr site were prepared with a systematic order to obtain polycrystalline samples of $(Sr_{1-x}Ca_x)_2IrO_4$ with nominal concentration of $x = 0.02$, 0.05, 0.07, and 0.10; and $(Sr_{1-x}Ba_x)_2IrO_4$ with $x = 0.05$, 0.10 and 0.15. The reactants used were IrO_2, $SrCO_3$ and CaO (for Ca substitutions) or $BaCO_3$ (for Ba substitutions). These were mixed in a stoichiometric ratio and were ground with a mortar to make the mixture more homogeneous. Samples containers used were Al_2O_3 (high purity alumina) crucibles which have an inert reaction and high melting point (2054°C) to avoid contamination for the reaction process. We chose a previously designed calcination process where we have already obtained a high quality parent sample at our laboratory facilities [22]. The programmable heating rate was 200°C/h until it reached 1100°C and it was maintained for 24 h. Then, it was cooled to room temperature at the rate of 4°C/min. Fig. 4.1 shows the schematic calcination process with our furnace.

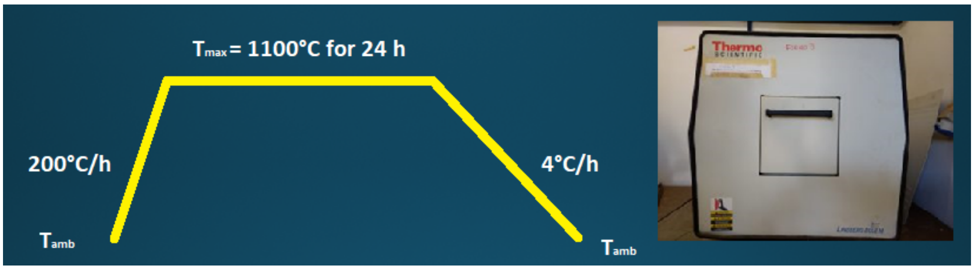

Figure 4.1: Programmable calcination process with the furnace available at the Laboratory of Materials and Devices (LMD-IFGW-UNICAMP).

4.2 Powder X-ray Diffraction

Powder X-ray diffraction experiments provide accurate information about the structure and content of materials. Usually powder diffraction patterns are collected in a one-dimensional independent variable, which collects the tree dimensional reciprocal lattice of the crystal. This simplest variable is used to represent the Bragg angle where a set of discrete intensities or Bragg reflections manifest the presence of a singular crystalline phase. Therefore, if structural parameters such as atomic positions, cell dimensions or population of different sites in a particular crystalline phase are altered, these will have a direct effect at their relative intensities or at the Bragg peak positions which correspond to an specific crystalline phase.

Our powder X-ray diffraction measurements were performed at ambient conditions using a Bruker D2 Phaser diffractometer (GPOMS laboratory) with Bragg-Brentano focusing geometry using a Cu $K\alpha_{1,2}$ radiation source. Fig. 4.2 shows the equipment and its schematic diffraction geometry $\theta - \theta$.

The structural characterization was performed using the X-ray diffraction pattern and the Rietveld refinement technique. The latter method is an approach of least squares that uses a theoretical model that is refined until it better characterizes the X-ray data measured. These X-ray powder pattern characteristics such as the height, width, position and line profile are a convolution result of structural parameters from the sample and instrumental factors. Here, we used a software called GSAS+EXPGUI suite and a modified

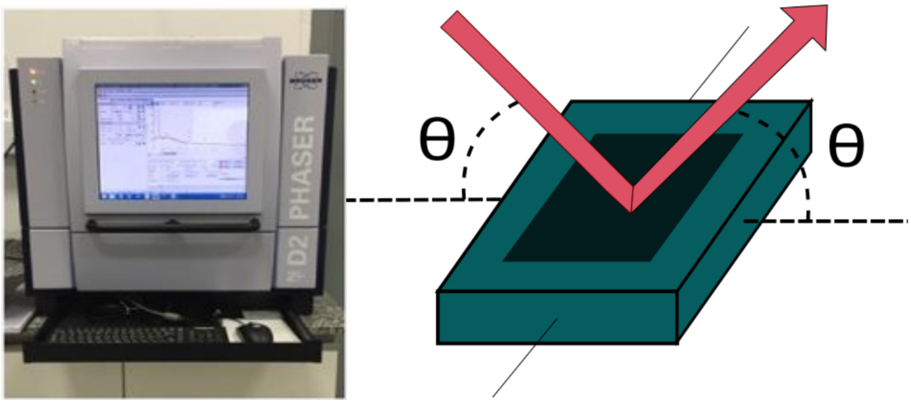

Figure 4.2: a) Bruker D2 Phaser Diffractometer at GPOMS and b) the schematic representation of the Bragg-Brentano geometry where the source radiation and the detector are rotated simultaneously as depicted with the arrows ($\theta - \theta$).

pseudo-voigt profile function with an asymmetric factor to refine the theoretical model [45].

4.3 DC-Magnetization

The DC-Magnetization from a sample is defined as the induction of a sample's net magnetic moment by an applied magnetic static field. The employed instruments to extract the magnetization in this project use a principle based on Faraday's law at the vibrating-sample magnetometer (VSM). Fig. 4.3 shows an schematic diagram of a VSM system where the sample is coupled to a mechanical linear motor inside a cryogenic chamber. The induced magnetization effect of the applied magnetic field is collected with a high precision sensor depicted as pick-up coils. The induced *emf* is proportional to the analyzed sample's magnetic moment M which is contrasted with a reference magnet that owns a well-known magnetization M_{ref}. These magnetometers are adapted for high precision measurements with a temperature controlling system.

In the context of this study, there is a correlation of the Ir-O-Ir angle geometry distortion and the canted magnetic moment proper to the iridate's $J_{eff} = 1/2$ system [6]. Thus, the chemical substitution or "chemical pressure" is expected to tune the geometry of the lattice and it might modify the tilt magnetic moment as well as its exchange interaction. The parent sample has a critical magnetic field $\sim$ 0.15 T which induces a net magnetization by aligning its canted moment to the field direction at the base plane of the lattice [46]. Here, we used a PPMS-14T and a SQUID MPMS3 Quantum Design

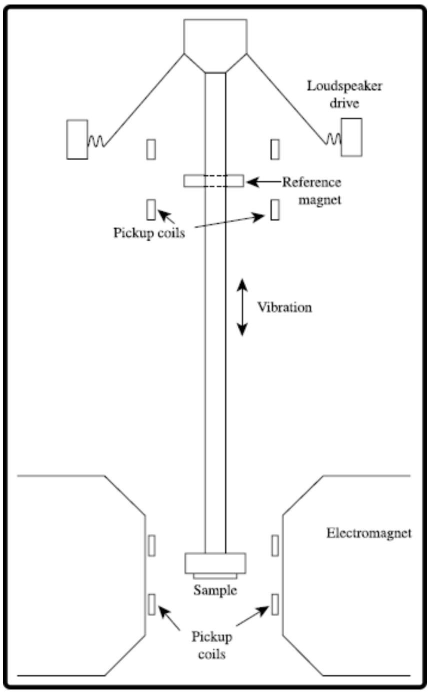

Figure 4.3: Schematic representation of a vibration-sample Magnetometer (VSM). *Figure adapted from ref.* [47].

magnetometers with an applied static field $H = 0.5$ T. We measured the polycrystalline samples within the Zero Field Cooling (ZFC) and Field Cooling (FC) modes, with a base temperature of 3 K.

4.4 Raman spectroscopy

Since Sir Chandrasekhra Venkata Raman discovered the phenomenon of inelastic light scattering in 1928, technological advances on Raman spectroscopy components let to a scientific community a wide variety of excitation sources, sample environment controlled systems, holographic gratings coupled to the monochromator collected system, and detection systems; and it made capable to achieve a sensitive high resolution technique.

An schematic instrumental layout distribution of Raman spectroscopy is observed in the fig. 4.4. This figure also represents some devices that we used to study the previously mentioned low energy excitations at sec. 2.3.2. The incident and scattered light were disposed in a quasi-backscattering geometry. We used a monochromatic radiation source of a diode pumped laser (DPL) with a single continuous wavelength 532 nm carefully coupled to a Volume Bragg Grating (VBG) element in order to achieve an stable narrow linewidth laser and improving the signal noise ratio. Then, these beamline was aligned and guided with a set of mirrors (M) and a lens (L) to focus the incident light to a sample. The scattered light was focused with a lens and filtered to the entrance slot with notch filters (NF) that reduces the elastic scattering. We employed a high resolution triple-grating T64000 Jobin-Yvon Raman spectrometer with 1800 mm^{-1} gratings monochromator and a liquid-nitrogen-cooled multichannel CCD detector system.

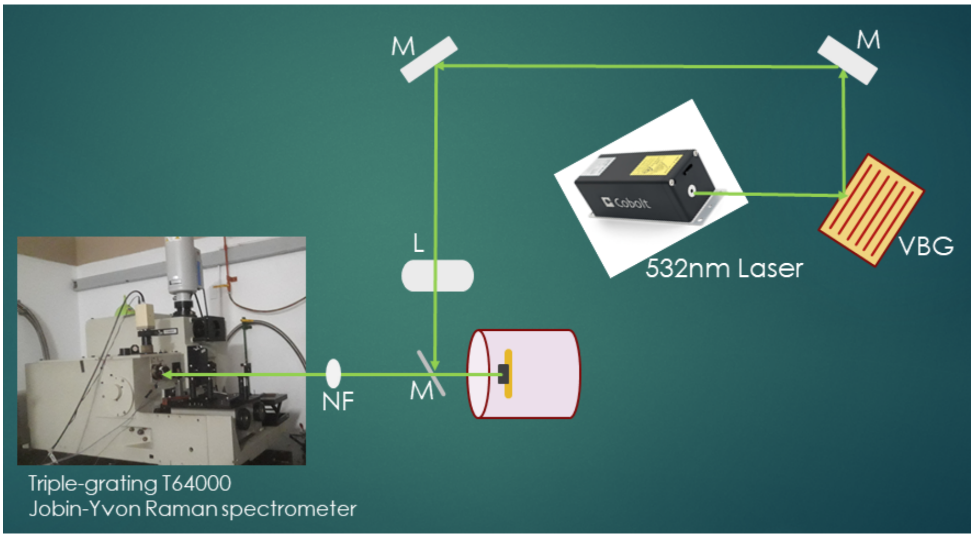

Figure 4.4: Schematic representation of the components in a Raman spectroscopy experiment.

In order to mount our synthesized powder samples, each sample was packed in pellets and sinterized for 24 h at 1100° in a furnace. Small cut pieces of samples ($\sim$ 1 mm) were pasted to a Cu holder attached to cold finger inside of a closed-cycle helium cryostat with a base temperature of 17K. Near the holder, there is a sensor CERNOX CX-1050-CU-1.4L, which was previously calibrated to a temperature controller system Lakeshore C340.

Finally, in the context of the temperature dependent Raman scattering for each sample, we employed a plasma line $\sim$ 480 cm^{-1} and a reference sample of Si to rectify some slight mechanical backlash of the wavenumber reading of the spectrometer which was centered at 340 cm^{-1} to measure the Stokes scattering.

Chapter 5

Results and Analysis of single layer Iridates $(\mathrm{Sr}_{1-\mathrm{x}}\mathrm{A}_{\mathrm{x}})_2\mathrm{IrO}_4$ (A = Ca, Ba)

Many experimental and theoretical studies about the single layer iridate $\mathrm{Sr_2IrO_4}$ indicate evidence where the strong spin-orbit coupling plays a crucial role along the $\mathrm{J}_{eff} = 1/2$ pseudospins and the lattice degrees of freedom for the realization of its magnetic order. In particular, pseudospin-lattice coupling would be important for the stabilization of its magnetic behavior. Besides that, studies applying of hydrostatic, strain or chemical pressure have showed anomalous behavior indicating uncommon magnetic and transport properties.

Therefore, it becomes essential to understand the critical role of subtle structural distortions on the physics of iridates. Thus, identifying elementary excitations and describing the low energy excited states could probe the hierarchy of energy interactions that could dictate the low-energy Hamiltonian. In this way, these lead us to tune the ground system with chemical substitution on the Sr site without extra electronic carriers doping to the $\mathrm{J}_{eff} = 1/2$ state.

Given that, we are going to present the impact of their static structure, magnetization and local dynamics by X-ray diffraction, DC-magnetization and Raman spectroscopy, additionally to an intuitive modification of the Ir-O-Ir angle or the volume change by chemical pressure with Ca and Ba. Nonetheless, we show anomalous behavior of their magnetic and temperature properties at the low energy excitations.

5.1 X-ray Diffraction Analysis

Firstly, we characterize our synthesized samples by X-ray diffraction in order to identify their phase fingerprint. There, our results showed a miscibility limit of Ca/Ba at Sr site for $(Sr_{(1-x)}A_x)_2IrO_4$ synthesis with a concentration limit of $x \sim 0.10$. Then, we analyzed with the Rietveld method to extract the structural parameters that could best fit to our samples lattice properties. There, it is observed a volume tuning by the chemical pressure, although a non-linear compression and expansion of the lattice cell parameters are also displayed.

The collected X-ray diffraction patterns (I vs 2θ) of the samples are shown in Fig. 5.1. It is noticed that the principal phase obtained on each sample has the same characteristic tetragonal symmetry of the parent system Sr_2IrO_4. However, there were minor additional peaks with no Bragg position correspondence to the parent sample marked with *. This impurity phase has been already reported [48] and we also identified the phase $Sr_3CaIr_2O_9$ on our samples which we try to synthesize with 7% and 10% concentration of Ca at the Sr site. Moreover, the diffraction patterns of the samples with Ba showed a left shoulder at their higher intensity peaks which could be observed at the inset of figures 5.3. In order to identify the possible origin of this shoulder, we performed other measurements with an X-ray diffractometer D8 Advance Bruker from the Multiuser Laboratory (LAMULT-IFGW-Unicamp) which has a better angular resolution using a point detector. There, we identified a single crystalline phase without impurities for samples with 5 and 10% of Ba (see fig. 5.2) which expose narrower Bragg peaks and also no sign of the left shoulder observed with a D2 diffractometer. We also tried to synthesize a sample with higher concentration of 15% Ba, because there were no reports in the literature. However, the X-ray diffraction led major unidentified impurity peaks with a higher background signal that would come from a non crystalline phase *that we avoided to expose here*. Thus, we could indicate that chemical synthesis with substitution of Ca and Ba ions showed a miscibility limit for both at $x \sim 0.10$ on the Sr_2IrO_4 crystalline system.

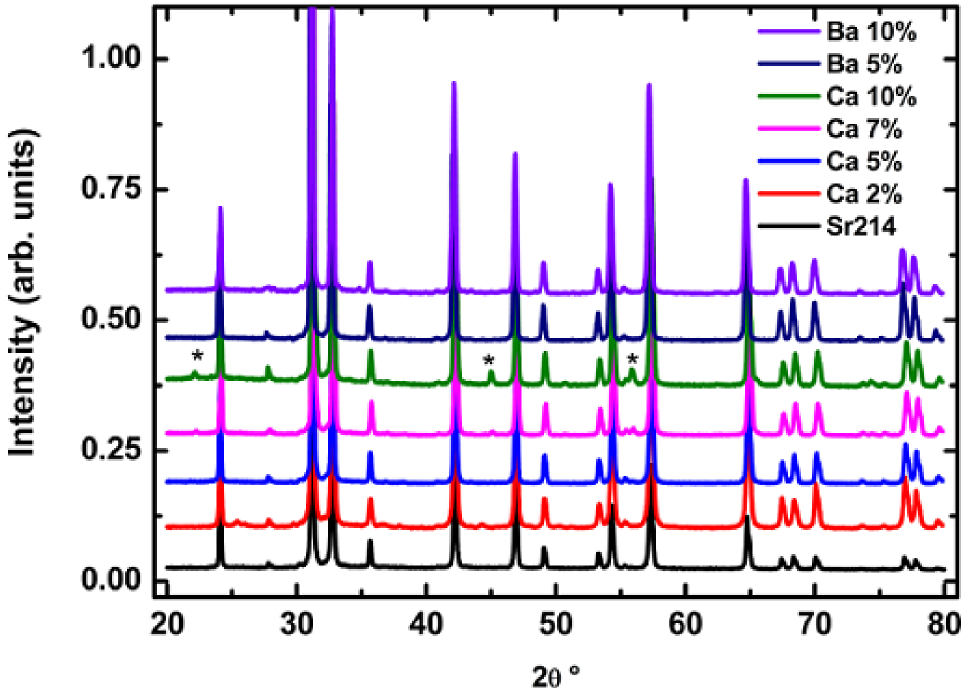

Figure 5.1: X-ray powder diffraction profiles ($\lambda = 1.54$ Å) of the investigated samples.

We analyzed the X-ray data using $I4_1/acd$ crystal symmetry group. Before the Rietveld refinement process, we characterized the instrumental contribution using a reference sample of Alumina. Thus, we could start gradually the least squares refinement using the same instrumental parameters and an asymmetric pseudo-voigt lineshape [49]. Figure 5.3 shows the experimental and calculated X-ray diffraction pattern with their residual difference for each sample. We could observe qualitatively a good enough fitting without considering to Ca/Ba concentration fraction and O^{2+} atoms positions in the refinement process.

Fig. 5.4 shows the contraction and expansion of the lattice cell parameters and the unit cell volume obtained from the refinement. We observe that the Ca and Ba substitutions at the Sr site contract and expand the unit cell, respectively. At the same time, it is important to note the non-linearly dependence on x of these parameters for a later discussion, where also anomalous magnetization and low energy excitations results are observed by the cation substitution at Sr site.

The "chemical pressure" responsible to the expansion and compression of the lattice could be related to an analogous hydrostatic pressure, such as we drawn on the previous study of our group to estimate an hypothetical hydrostatic pressure [22]. Thus, using

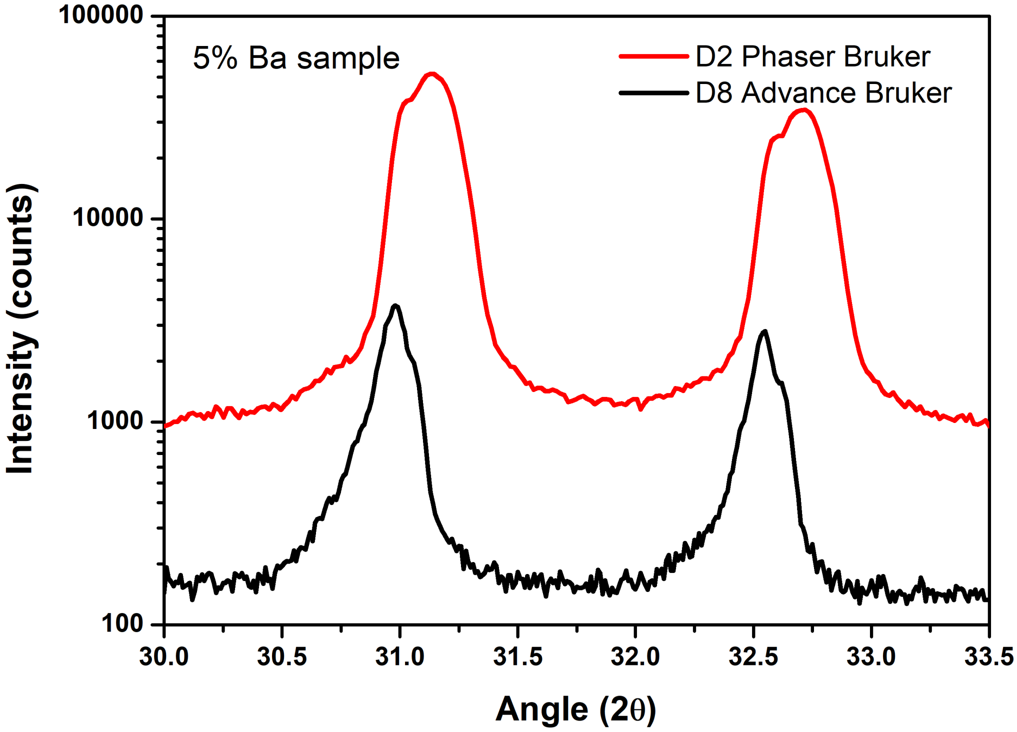

Figure 5.2: Comparative x-ray diffraction measurements of the sample with 5% of Ba st Sr site using D2-Phaser and D8 Advance Bruker diffractometers.

the previous volume pressure dependence as a reference data (see fig. 5.5(a)), we could extrapolate an analogous external pressure for the "chemical substitution" of Ca and Ba at our samples. It is used a linear function to obtain a volume compressibility constant which we could put on to assign an analogous pressure to our cell volume results at fig. 5.4 (c). As a result, figure 5.5(b) shows an hypothetical external pressure applied equivalent to the modified unit cell volume and related to the synthesized samples. We could thus estimate an equivalent applied external pressure around ±12 kbar relative to the compression and expansion on our samples. Later, this relative pressure is discussed at sec. 6 about the low energy excitations behavior.

5.2 dc-Magnetization

As mentioned at section 2.2, the system Sr_2IrO_4 presents a canted Antiferromagnetic order. Despite this, the application of a magnetic field could drive a ferromagnetic transition order above a critical field $H_C \simeq 0.2$ T aligning the canted moment to the field direction.

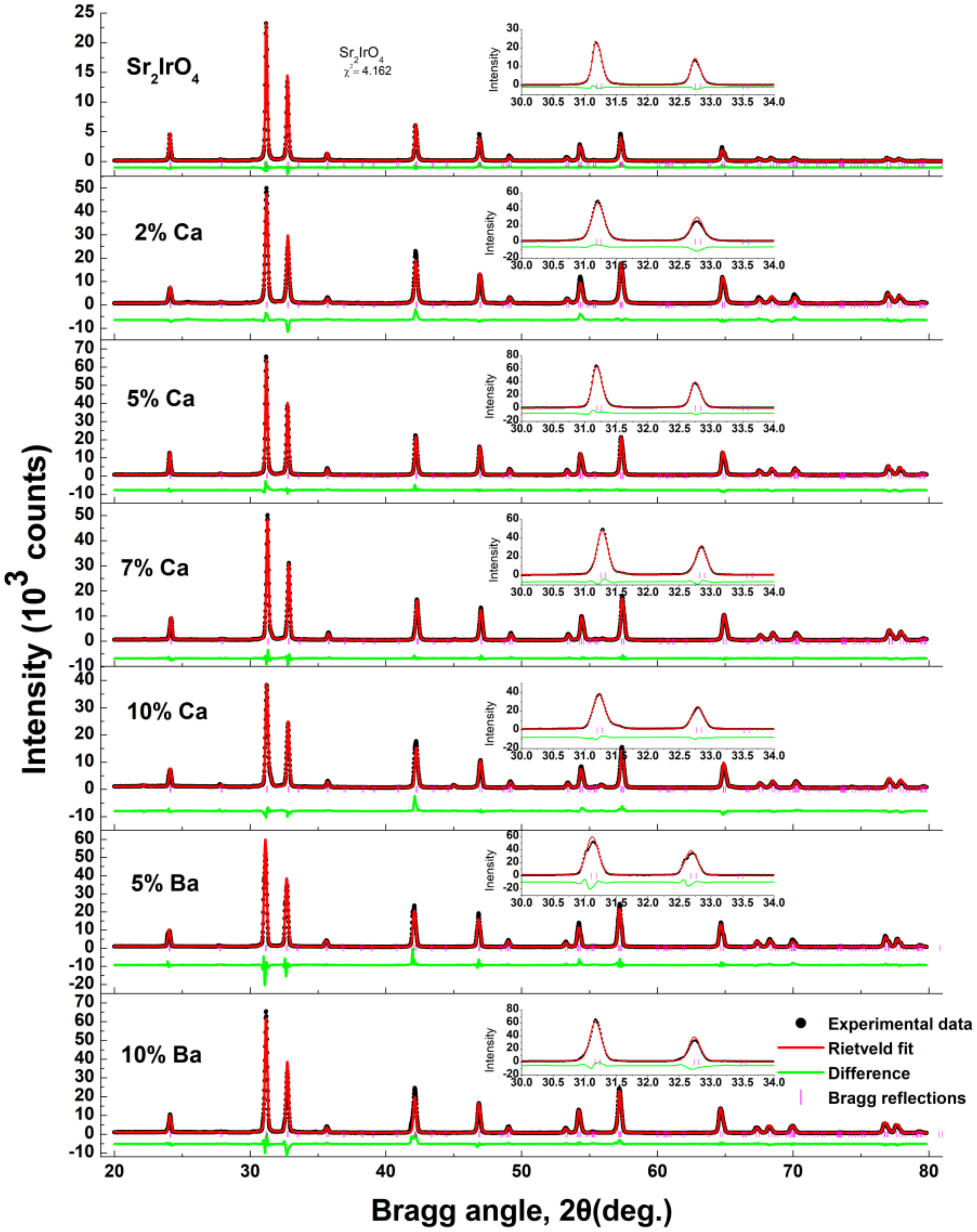

Figure 5.3: Observed and calculated X-ray diffraction pattern from all the samples including a zoom in of its more intense peak ($\lambda = 1.54$ Å).

Thus, the performed Field Cooling (FC) and Zero Field Cooling (ZFC) magnetometer modes with a magnetic field H = 0.5 T would mainly measure the temperature dependence of the resulting canted magnetic moment that is intrinsically related to the Ir-O-Ir lattice

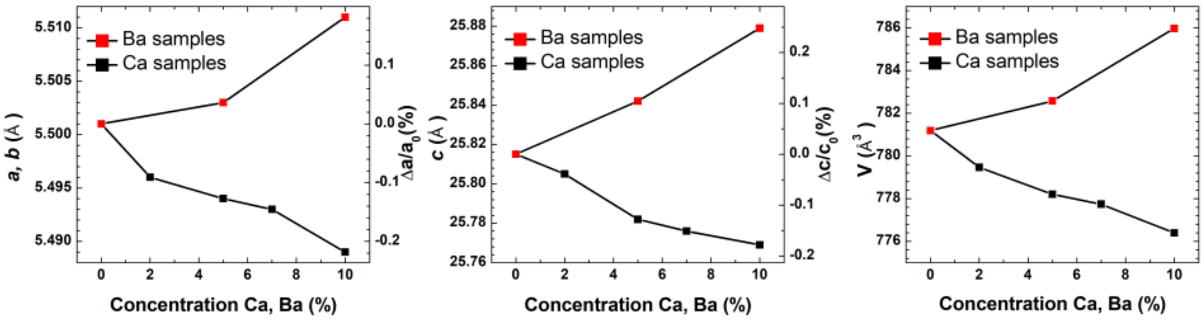

Figure 5.4: a, b and c lattice parameters and unit cell volume V as a function of Ca or Ba concentration at Sr site.

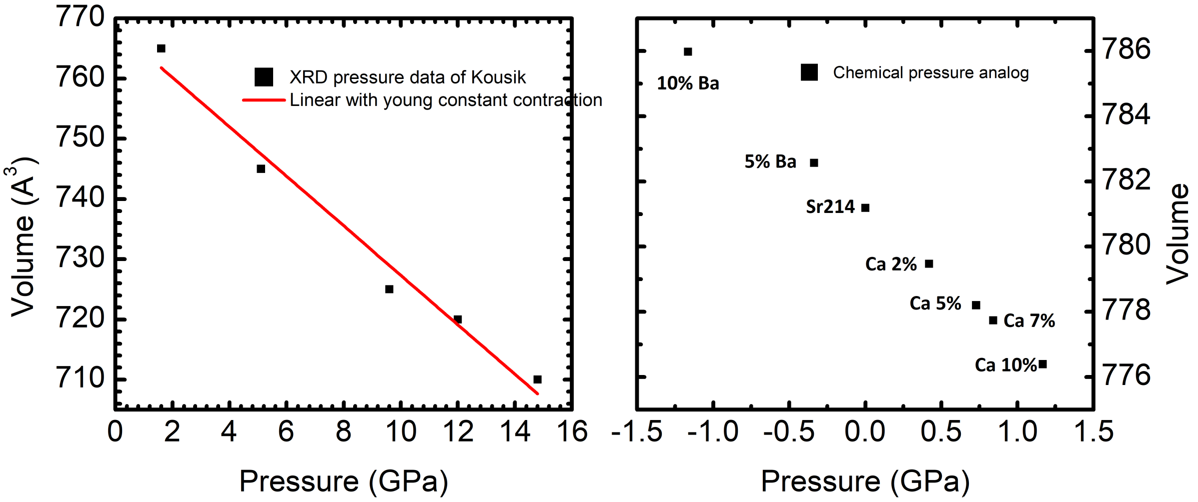

Figure 5.5: a) Linear interpolation of pressure contraction with hidrostatic compression [22], b)Relative pressure dependence of each sample with the extrapolated compression coefficient.

distortion. Besides that, our results showed also non linear behavior with the chemical pressure or the unit cell volume.

Figure 5.6(a) shows the magnetization temperature dependence curves ($M \times T$) for the investigated samples at the Field Cooling (FC) magnetometer mode. First, we observed that the parent sample reaches a saturated net magnetization of 0.045 μ_B/f.u. at the base temperature which is consistent to the moment projection of the Ir^{4+} equivalent to $\mu = 0.049(2)\mu_B$ value [12]. Then, we got the magnetic transition temperatures by differentiating the magnetic curves (dM/dT) where our $\mathrm{Sr_2IrO_4}$ sample shows a $T_N \sim$ 236 K (see fig. 5.6(b)). Thus, our polycrystalline sample shows a high quality magnetic properties consistent with previous studies [9, 10, 46, 50, 51, 52].

Furthermore, $(\mathrm{Sr}_{(1-x)}\mathrm{Ca}_x)_2\mathrm{IrO}_4$ samples with $x = 0.02, 0.05, 0.07$ presents a diminished

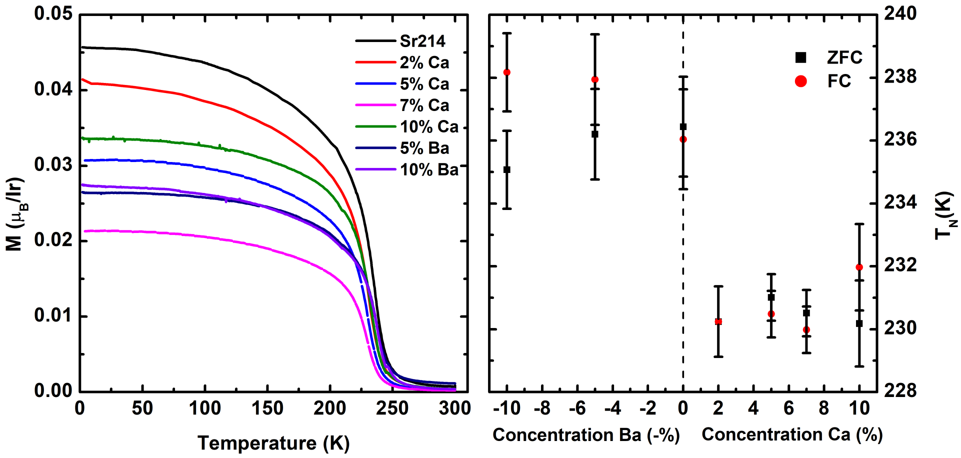

Figure 5.6: (a) Temperature-dependence of the magnetization of the investigated samples, taken under field cooling with $H = 5$ kOe. (b) Magnetic ordering transition temperatures T_N defined as the minimum of the dM/dT curves.

net moment while it is increased the Ca concentration, meanwhile, the sample with $x = 0.10$ has an intermediate magnetic moment between samples with $x = 0.05, 0.07$ and it did not follow the same tendency (Fig. 5.6(a)). In case of $(\mathrm{Sr}_{(1-x)}\mathrm{Ba}_x)_2\mathrm{IrO4}$ samples with $x = 0.05, 0.10$, they have a lower net magnetic moment from the parent sample but also similar values between each other, and are closed to the net magnetic moment whose Ca concentration is $x = 0.05$. Furthermore, the samples' transition temperature depicted at the figure 5.6(b) shows a consistent value where only samples with Ca got a little reduction from $\sim$ 237 K to $\sim$ 230 K. Nonetheless, the Zero Field Cooling measurements (fig. 5.7) show a different behavior at lower temperatures where samples with Ba have a lower magnetization irreversibility from parent and samples with Ca.

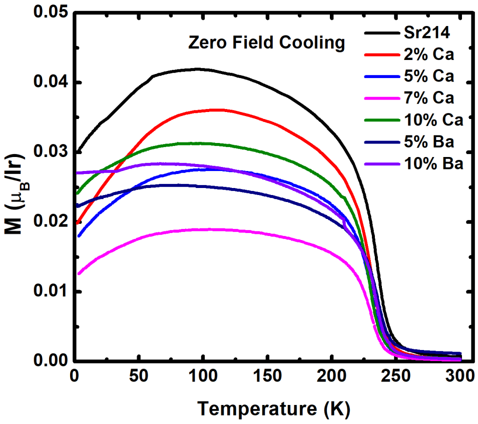

Figure 5.7: The investigated samples' temperature-dependence of the magnetization taken under Zero Field Cooling with an applied magnetic field $H = 5$ kOe.

In summary, our samples showed evidence of similar magnetic properties in comparison to previous studies of polycrystalline samples [50, 53, 54]. However, the obtained reduced magnetic moment even with positive or negative "chemical pressure" to the parent sample could indicate a more complex explanation for these samples properties whose ϕ angle distortion (Ir-O-Ir) and the magnetic tilt are expected to be correlated within the *compass model* [6]. These non-linear and contrast results will be discussed in chapter 6.

5.3 Raman Scattering

Having already the characterization of its structure and magnetic properties, we developed a Raman study of the parent sample Sr_2IrO_4 and the samples under "chemical pressure". We performed the Raman spectroscopy measurements across a controlled temperature range of 25-400 K (see sec. 4.4 for the experimental details). Thus, we are going to show in this section the low energy excitations behavior above the chemical pressure and the temperature analysis.

First, we find important to describe briefly again their principal characteristics of these low energy excitations in order to analyze and interpret our results. At sec. 2.3.2, we described the phonons' symmetry and their mechanical representation, that we are dealing in this work (see fig. 2.9 for the mechanical representation of the phonons' symmetry). Also, we described the single magnon excitation at the Brillouin center $\mathbf{q} = 0$ at sec. 2.2.1. Thus, ab-initio calculations of the lattice dynamics described the observed phonons: M_1 as superposition of a libration mode of IrO_6 octahedra combined with an in-phase displacement of Sr site along c-axis and a pure Sr vibration mode; M_2 as a libration mode of the IrO_6 octahedra around the tetragonal *c*-axis; M_3 as a bending mode of oxygen's squares (O-Ir-O) at the IrO base plane; and M_4 as a stretching mode of the apical oxygen ions along the *c*-axis [22]. In addition, the magnetic excitation M_0 was ascribed by a lattice-pseudospin coupling at the base plane that lift this energy gap [18].

In relation to these reports, the figures 5.8 [(a)-(f)] illustrate the Stokes Raman response of our samples at low and near the magnetic transition temperatures (T = 25, 240 K). We applied a correction to the differential cross section proper to the Bose-Einstein factor $[1 + n(\omega)]$, where $n = 1/[exp(\hbar\omega/\mathrm{K}_B\mathrm{T}) - 1]$ represents Bose's distribution number. Thus, the parent sample's Raman spectra (Fig. 5.8 (a)) shows the four major phonon structures labeled as M_1-M_4, and the additional low frequency excitation at 25

K labeled as M_0. These frequencies were centered at $\sim$ 20, 185, 275, 395, and 565 cm^{-1} for the respectively excitations M_0-M_4 at 25 K. In addition, figures 5.8 (b)-(f) show the Raman spectra for samples with concentration $x = 0.05$, 0.07 and 0.10 of Ca and samples with concentration $x = 0.05$ and 0.10 of Ba at Sr site at 25 K and 240 K. This sequence of spectra shows an almost flat baseline with a little excitation between M_2 and M_3 accounted for all the samples at 25K. Thus, the described excitations energies consistent with previous studies on the parent sample, and no traces of impurities on our samples above chemical pressure are grounds that also support a good crystalline quality holding the same crystal symmetry on our samples [16, 17, 21, 22].

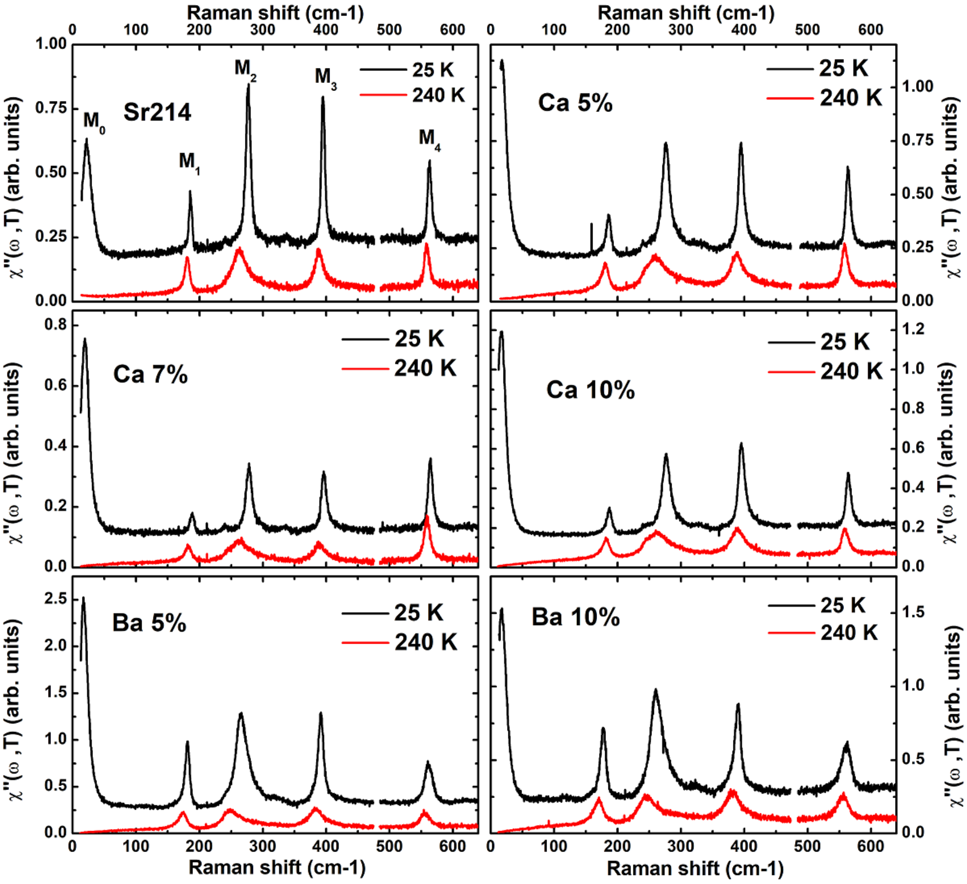

Figure 5.8: Raman response for the samples investigated in this work, at 25 and 240 K.

Bearing in mind the different origin of these low energy excitations, we split and organized into subsequent subsections the chemical pressure tuning effect and the temperature analysis.

5.3.1 Optical Phonons M_1-M_4

We analyzed the energy and lifetime of the optical phonons M_1-M_4 and the temperature dependence. Thus, we extracted the vibrational frequency energies ($\lambda^{-1}cm^{-1}$) and lifetime (inverse proportional to the peak's linewidth) of the symmetric peaks M_1, M_3 and M_4 using a Lorentzian function [55]. Phonon mode M_2 owned an asymmetric profile which indicates an interference between a continuum of excitations and this optical phonon. Thus, we extracted its vibrational parameters by making use of a Fano lineshape, $I(\omega) = I_0(q+\epsilon)^2/(1+\epsilon^2)$ where $\epsilon = (\omega - \omega_0)/\Gamma$, ω_0 is the mean frequency, Γ is the linewidth, and $1/q$ is the asymmetry parameter [27]. Then, we could trace these vibrational properties of each phonon mode for each sample between a range temperature of 17-400 K.

First, it is important to describe the tunning effect across the lattice excitations M_1-M_4 at 25K in the tables 5.1 and 5.2. There, the sample with 2% of Ca (x=0.02) presents frequency values a bit lower and similar linewidths to the parent sample, but samples with Ca concentrations of 5%, and 7% showed a slight phonon hardening and increased linewidths compared to the parent sample. However, when concentration is x=0.10 for Ca, it showed an intermediate behavior between samples with x=0.05 and 0.07 of Ca. On the other hand, the samples with Ba concentrations of 5 and 10% showed an abrupt phonon softening energy compared to the parent sample. Furthermore, the linewidths of phonon modes M_1 and M_3 presents similar values to samples with 5, 7 and 10% of Ca. In contrast, the M_2 and M_4 phonons' lifetime of our samples with Ba specially showed a higher broadening. In particular, the energy tuning effect (see table 5.1) indicates no direct implication of the Grüneisen's law, which would modulate the energies as $\Delta\omega/\omega \propto \Delta V/V$. Despite this anomalous energy and broadening tuning effect above chemical pressure, we discussed at sec. 6 a possible proper perturbation in the local structure of our synthesized samples with low concentration of Ca and Ba.

At sec. 3.2.1, we described the self energy variation $\Delta\omega_{anh}$ (frequency shift) due to phonon-phonon interactions beyond the harmonic approximation. Despite this, the pseudospin-phonon coupling interaction could also contribute to the optical phonon energy (see sec. 3.2.2 for more details) . In this way, we avoided our data below T_N ($T < T_N$) and applied the two-phonon decay model to estimate the anharmonic shift contribution $\Delta\omega_{\mathrm{anh},\sigma}(T)$ within the phonon modes σ (M_1-M_4) above T_N ($T > T_N$) at the paramagnetic

	M_1(cm^{-1})	M_2(cm^{-1})	M_3(cm^{-1})	M_4(cm^{-1})
Sr214	186.05(7)	276.86(4)	395.10(3)	563.19(5)
Ca 2%	185.98(7)	276.26(6)	394.40(4)	562.36(3)
Ca 5%	186.39(9)	275.61(8)	395.04(4)	563.88(4)
Ca 7%	188.3(1)	277.89(8)	396.47(6)	564.46(4)
Ca 10%	187.2(1)	275.82(8)	395.96(6)	564.27(5)
Ba 5%	181.56(4)	264.68(6)	391.54(3)	561.50(6)
Ba 10%	177.71(7)	259.26(9)	389.57(5)	560.6(1)

Table 5.1: Energy shift for each optical phonon mode at 25K for all the synthesized samples

	$\Gamma(M_1)$(cm^{-1})	$\Gamma(M_2)$(cm^{-1})	$\Gamma(M_3)$(cm^{-1})	$\Gamma(M_4)$(cm^{-1})
Sr214	5.4(2)	4.38(5)	6.4(1)	7.2(1)
Ca 2%	5.3(2)	4.79(6)	6.6(1)	6.9(1)
Ca 5%	9.1(3)	7.42(9)	10.2(2)	8.7(1)
Ca 7%	8.1(5)	5.72(8)	10.0(2)	8.6(2)
Ca 10%	9.8(3)	7.97(9)	12.3(2)	9.6(2)
Ba 5%	8.3(2)	11.3(8)	10.4(1)	15.2(2)
Ba 10%	10.4(2)	12.0(1)	12.1(2)	18.7(4)

Table 5.2: Linewidth for each optical phonon mode at 25K for all the synthesized samples

state of our samples. The following equation represents the frequency shift with a cubic anharmonic factor A_σ for the phonon mode σ [38]

$$\Delta\omega_{anh}(T) = A_\sigma[1 + 2/(\exp^{\hbar\omega_0/2K_BT} - 1)]. \tag{5.1}$$

Thus, figures 5.9(a)-(d) shows the solid curves taking into account a constant anharmonic factor A_σ that best fit the parent sample's frequencies above T$_N$ and we used this parameter for the phonon decay contribution at the samples above chemical pressure. However, we observed an anomalous phonon decay tendency for the mode M_2 at the samples with Ba.

The two phonon decay model let us identify the pseudospin-phonon coupling for the parent sample and the samples under chemical pressure, where figures 5.9(a)-(d) show the self energy ω and the associated phonon decay model for each sample. A previous Raman study of a single crystal Sr_2IrO_4 showed an evidence of strong "isospin-phonon" coupling by hardening each phonon mode M_1-M_4 below T_N [21]. The phonon modes M_3-M_4 showed even a higher hardening effect below T_N.

In order to observe how modes M_3 and M_4 change its temperature hardening below T$_N$, we subtracted the phonon' energies from the anharmonic contribution considering two

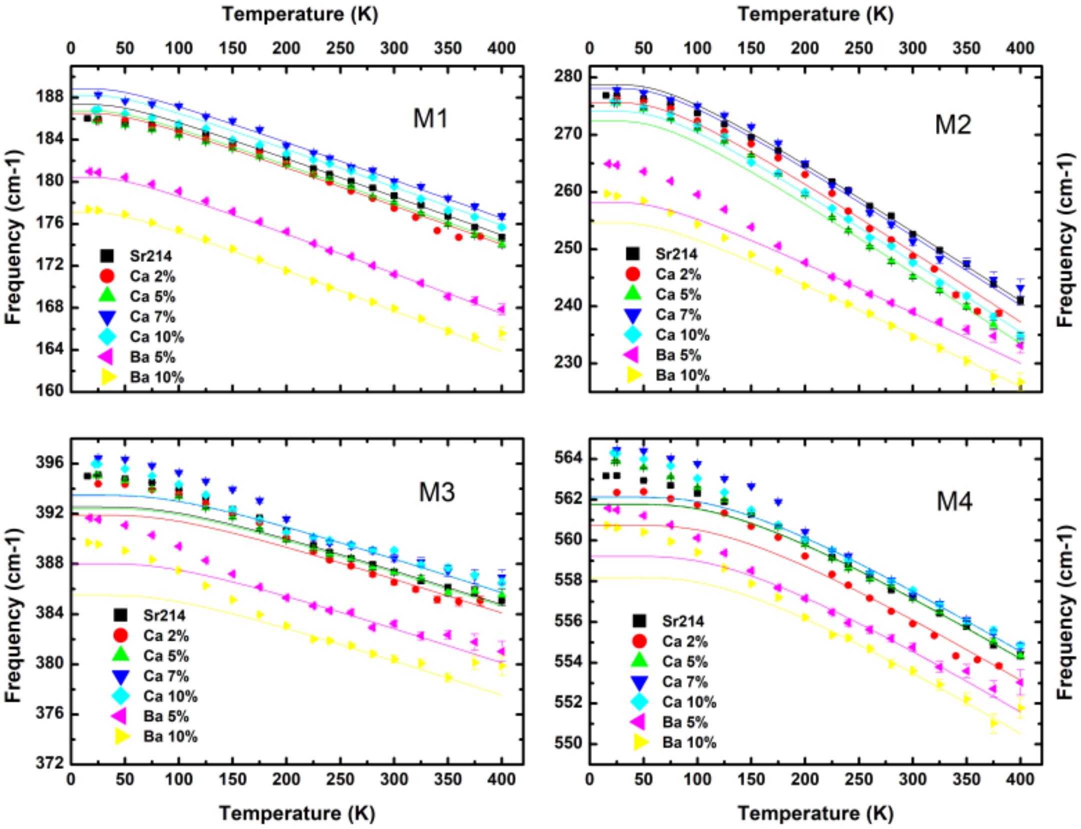

Figure 5.9: Temperature-dependence of frequencies of modes M_1-M_4, respectively, for the $[Sr_{1-x}(Ca,Ba)_x]_2IrO_4$ samples investigated in this work (symbols). The solid lines represent fits to the anharmonic two-phonon decay model (see text).

different approaches to get the anharmonic parameter $A_{\sigma=M_3,M_4}$. The first approach was taking into account an anharmonic parameter $A_{\sigma=M_3,M_4}$ that best fit the parent sample's frequency shift above T_N and the second approach was considering an anharmonic parameter $A_{\sigma=M_3,M_4}$ that best fit for each samples' frequency shift above T_N. Figures 5.10 and 5.11 show the phonon energy shift considering both mechanisms. There, we could observe a higher hardening effect for samples with Ba concentration below T_N compared to the parent sample using both analysis mechanism for the anharmonic parameter. On the other hand, samples with Ca show similar hardening for the bending mode M_3 but a higher effect for the apical mode M_4 comparing to the parent sample. Thus, samples with Ba could have indeed a reduced anharmonic constant, and samples with Ca seem to alter slightly the original potential energy. However, both samples with Ca or Ba shows a pseudospin-phonon coupling strength that have been favored for the apical mode M_4.

Furthermore, we used the two phonon decay model also to describe the broadening

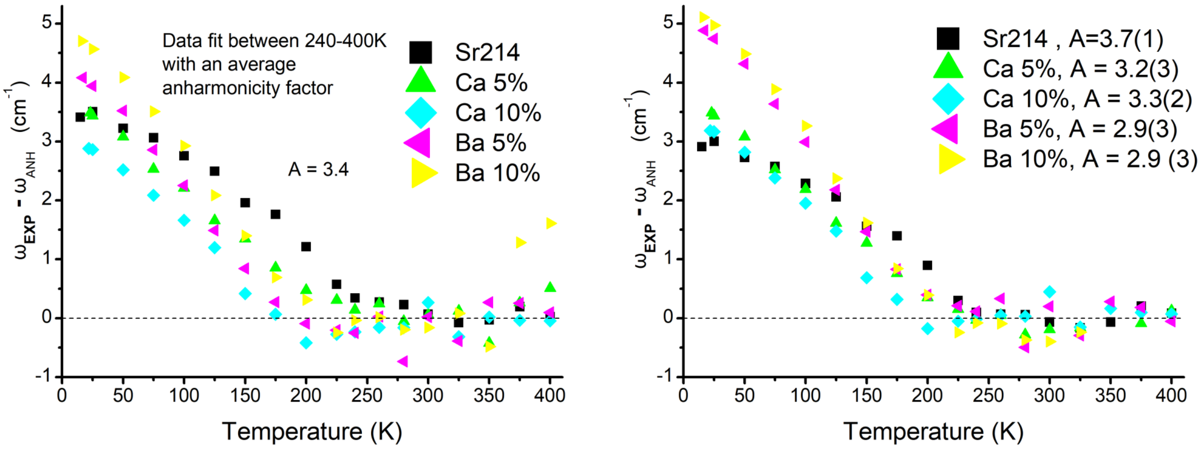

Figure 5.10: Phonon M_3 frequency shift due to the isospin-phonon coupling as a function of temperature considering a constant aharmonic factor A_{M3} (a) and its best fitted A_{M3} achieved above T_N for each sample (b).

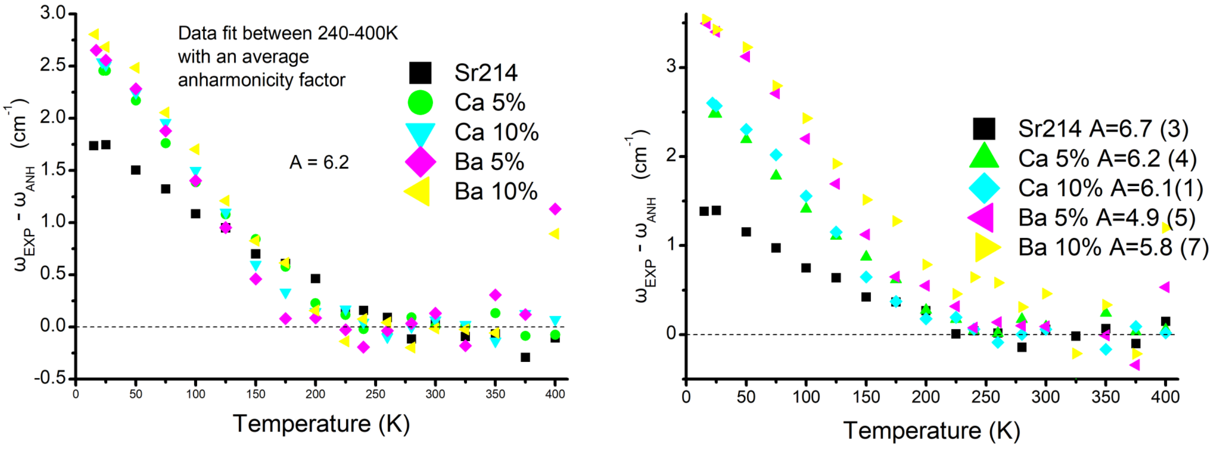

Figure 5.11: Phonon M_4 frequency shift due to the isospin-phonon coupling as a function of temperature considering a constant aharmonic factor A_{M4} (a) and its best fitted A_{M4} achieved above T_N for each sample (b).

behavior

$$\Gamma(T) = B_\sigma \left[1 + \frac{2}{\exp^{\hbar\omega_0/2K_BT} - 1} \right], \tag{5.2}$$

where B_σ is a broadening parameter of the σ phonon mode. Figure 5.12 shows the linewidth temperature dependence of each phonon structure. However, the broadening behavior respectively to each sample structure was not possible to fit with the same anharmonic parameter B_σ of the parent sample's. In addition, the loss of phonon correlation on mode M_2 and M_4 showed anomalous behavior that distinguishes samples with Ca or Ba where the latter have an stronger broadening.

In light of phonon mode M_2 presented a peculiar temperature- and composition-

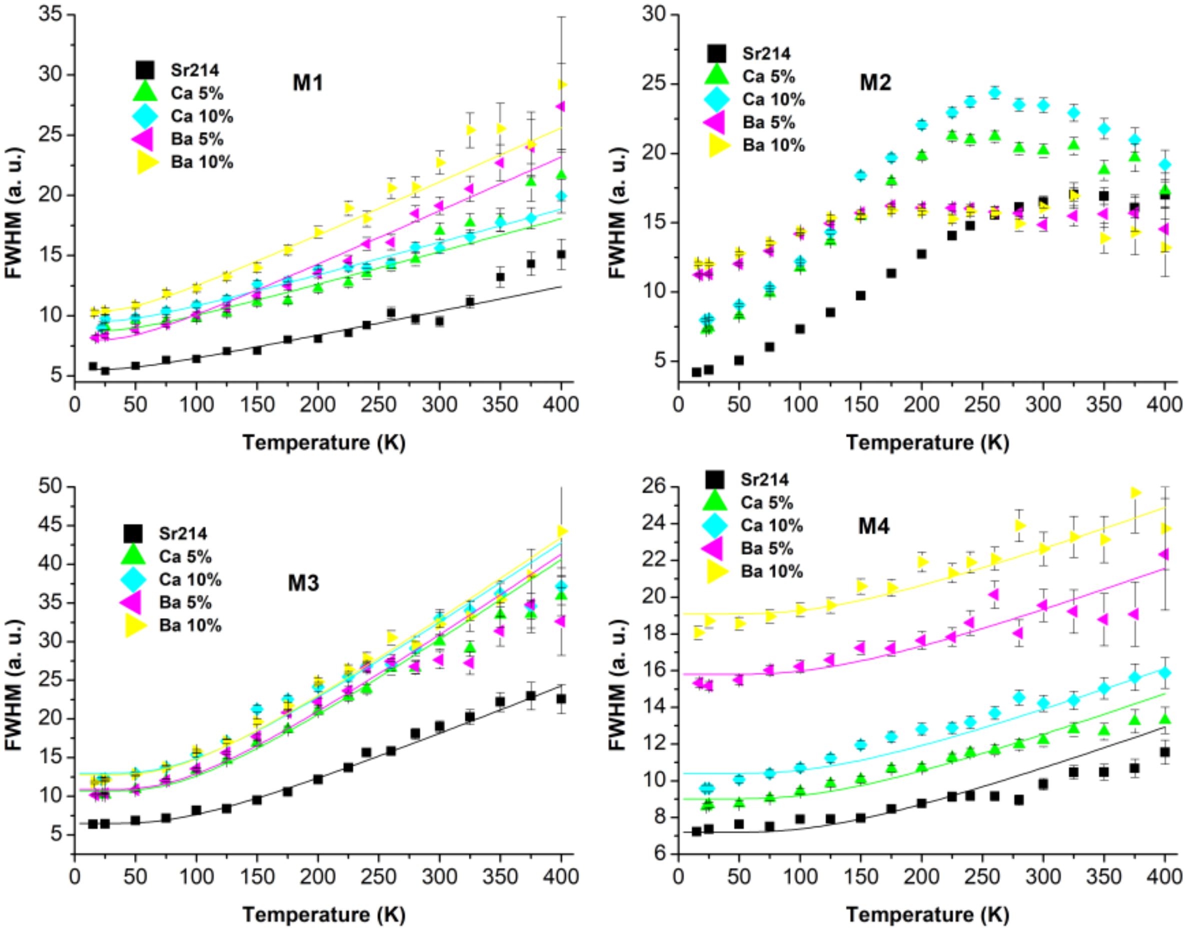

Figure 5.12: Temperature-dependence of linewidths of modes M_1-M_4 (a)-(d), for the $[Sr_{1-x}(Ca,Ba)_x]_2IrO_4$ samples investigated in this work. The solid lines represent fits to the anharmonic two-phonon decay model (see text).

dependent energy, broadening and Fano asymmetry (see figs. 5.13). that is not simply to interpret owning similar anharmonic effects or pseudospin-phonon coupling because fig. 5.13 shows there is an electronic continuum coupled to the phonon which increments on samples with Ca and Ba substitution. Then, Ba samples showed higher broadening and continuum-phonon coupling than Ca samples and these have intermediate values between Ba samples and the pure sample. In this way, it is also observed an anomalous broadening behavior by the temperature where it seems that the phonon correlation is stabilized when an electronic continuum coupling reach a top value. Also, the anharmonic decay on Ba samples seems to be diminished, however, it appears to have a similar decay as the other samples below T_N. Then, the mechanism of pseudospin-phonon, phonon-phonon and electron-phonon coupling seems to be competing with each other and it is modified differently even at the paramagnetic state. These anomalous results will be discussed later.

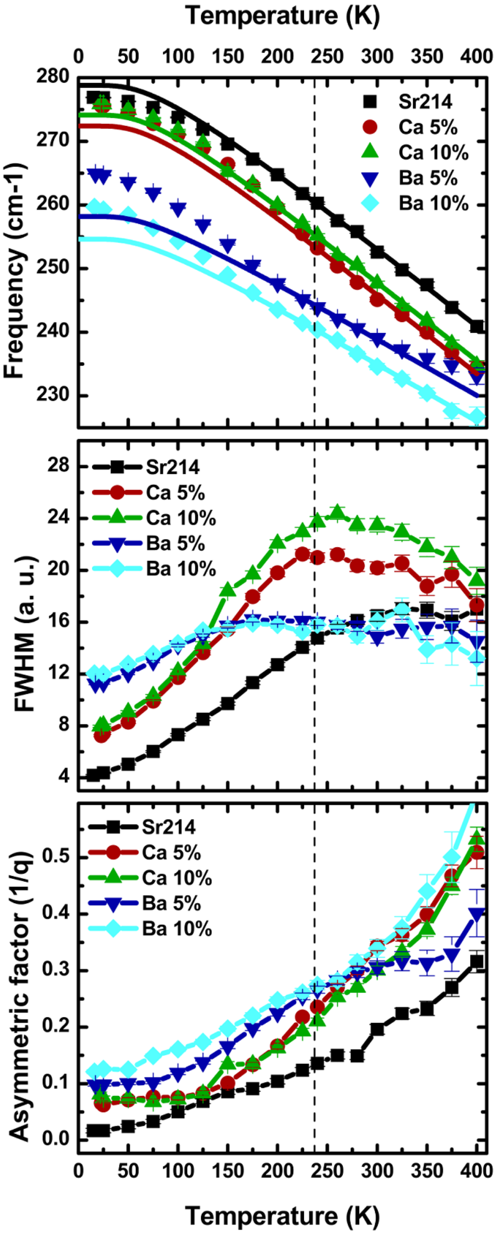

Figure 5.13: Temperature-dependence of frequency, linewidth and asymmetric parameter of mode M_2

In summary, the chemical pressure applied to our samples showed no direct relation between chemical-pressure and the phonon energies. Indeed, we observed anharmonicity, stronger pseudospin-phonon coupling, and electronic continuum-phonon coupling effects that are not proper to simple volume tuning. We discussed further these results at the following chapter.

5.3.2 Single magnon excitation (M_0)

Previous studies had already reported and identified the low-energy single-magnon excitation M_0 [16, 17, 18]. The magnetic scattering coming from the presence of this magnon excitation is a probe of the long range order state (AFM) below T_N. Thus, we looked at the single magnon excitation behavior under chemical substitutions.

The instrumental setup using notch filters and a triple grating spectrometer allow us to filter the elastic scattering and we were able to measure above $\sim$ 10 cm^{-1}. Even the high resolution near the elastic scattering, there we considered a correction to the wavenumber shift reading. Figure 5.14 shows a good quality data, although, it is important to note a loss of information due to the slight mechanical backlash of the spectrometer. Then, we employed a Lorentzian function so that we could analyze the temperature dependence.

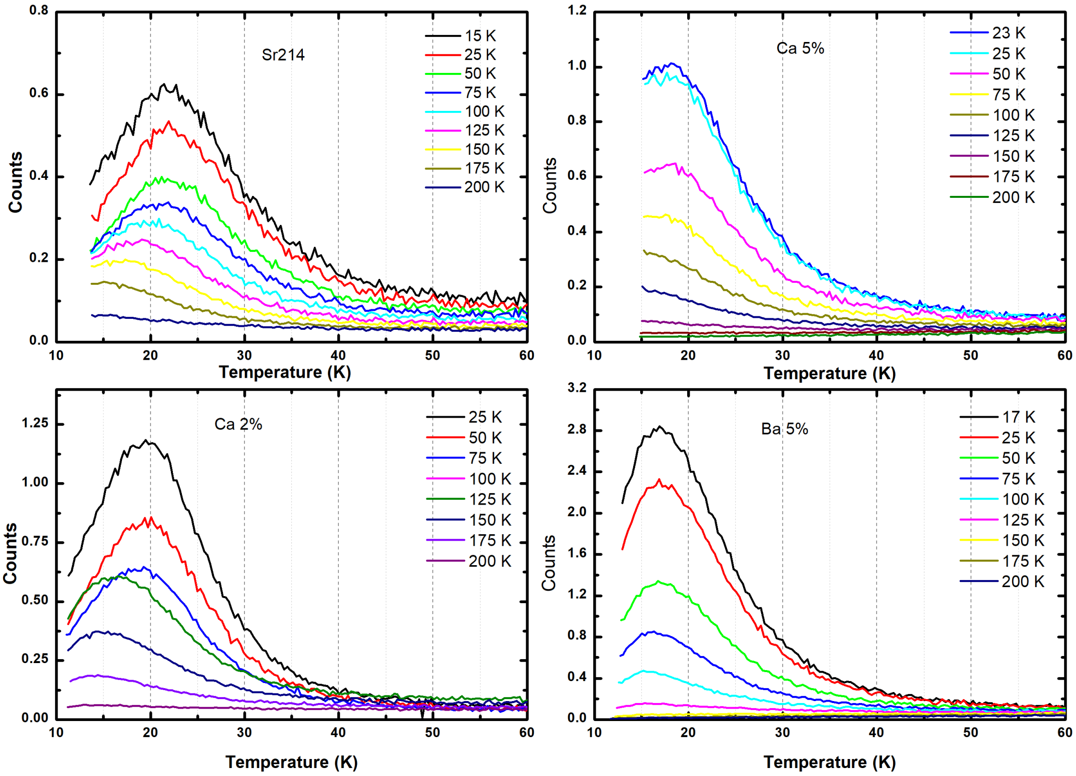

Figure 5.14: Single magnon spectra at different temperatures for the following samples: (a)Sr214, (b) Ca2%, (c) Ca5%, and (d) Ba5%

Figures 5.15(a) and 5.15(b) show respectively the excitation energy ω_{M_0} and linewidth Γ_{M_0} along the temperature dependence of the single magnon excitation M_0 for each sample. There, we observed a reduced energy and linewidth at 25 K for the samples above chemical pressure comparing to the parent sample. Particularly, the magnetic gap reduction of the sample with 2% of Ca is ~ 3 cm^{-1}, with 5% and 10% of Ca is ~ 4 and 5 cm^{-1}, whereas the sample with 7% of Ca is ~ 2 cm^{-1} comparing all to the parent sample. In contrast, the magnetic gap of the sample with 5% and 10% suffered a similar reduction of ~ 5 cm^{-1}. Thus, the volume modulation of the unit cell by the chemical pressure did not influence linearly the pseudospin-lattice coupling strength.

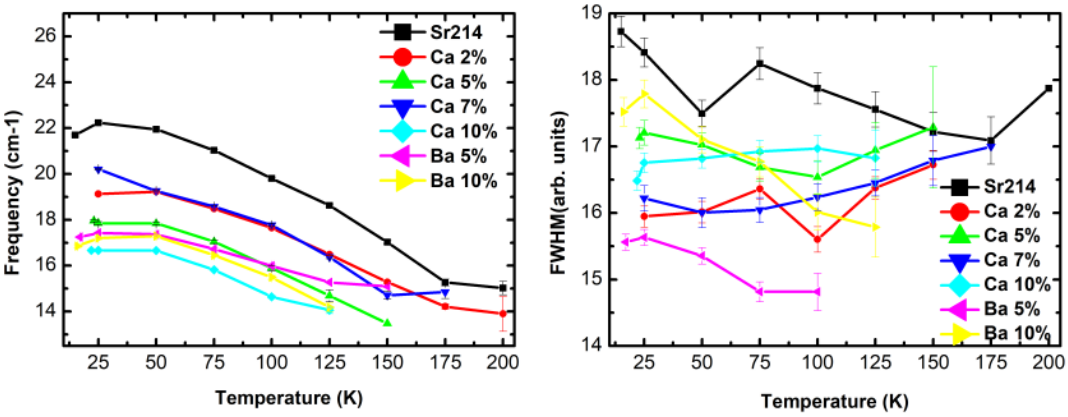

Figure 5.15: Frequency (a), linewidth (b) of the low-frequency Raman peak of all samples investigated in this work.

Furthermore, we observed a diminished magnon energy while the temperature is increased (fig. 5.15(a)). By the same magnon softening and the Raman shift reading limit, we could not detect the magnetic gap near T_N. Therefore, we modified our setup using more notch filters (NF) to avoid the elastic scattering and we turned down the laser power to 2.5 mW in order to avoid heating the sample. In addition, we centered the Raman spectrometer at the Rayleigh line through a single grating channel.

Figure 5.16 shows the single magnon excitation M_0 of Sr_2IrO_4 (a) and $(Sr_{0.93}Ca_{0.07})_2IrO_4$ (b) at different temperatures. Near the temperature T= 240 K, the fig. 5.16 also shows a quasielastic signal coming from the nearly closed magnetic gap. This confirms the long range magnetic order below the transition temperature $T_N \sim 240$.

Then, we made use of a damped harmonic oscillator (DHO) function to fit the peak profile: $I(\omega) = \frac{\chi_0 \Gamma_0 \omega \omega_0^2 (n+1)}{(\omega_0^2 - \omega^2)^2 + \omega^2 \Gamma_0^2}$; where, $n = 1/[\exp(\frac{\hbar\omega}{k_B T}) - 1]$, ω_0, Γ_0,and χ_0 are respectively the bose-einstein factor, magnon frequency, linewidth, and intensity [55]. Figure 5.17(a) shows the magnon energy softening for a sample with with 7% of Ca at Sr site and a temperature tendency similar to the parent sample. Figures 5.15(b) and 5.17(b) show

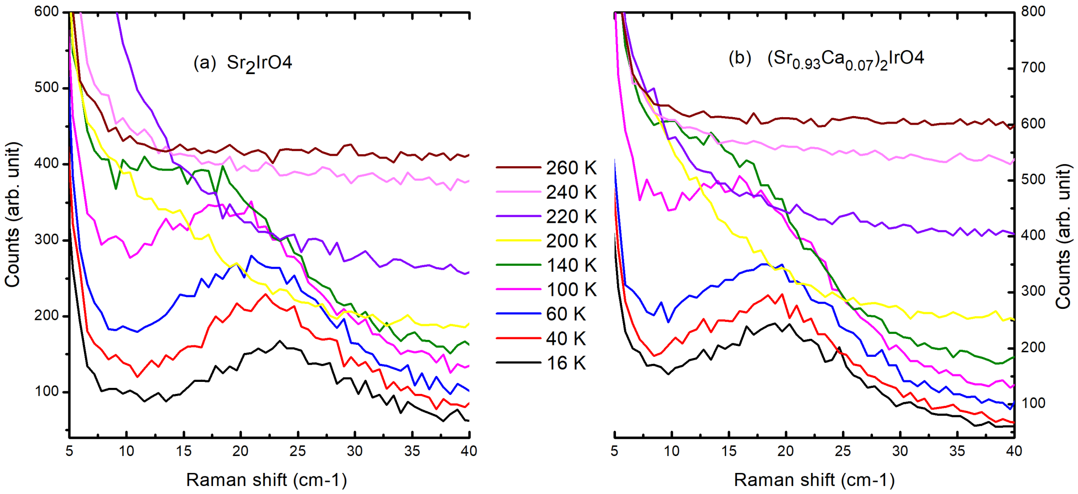

Figure 5.16: Single magnon spectra at different temperatures for the following samples: (a)Sr$_2$IrO$_4$, (b) (Sr$_0$.93Ca$_0$.07)$_2$IrO$_4$

both an slight sharpening of the spectra profile for the sample with 7% of Ca, however, it does not show an specifically temperature tendency. Nevertheless, fig. 5.17(c) exhibits the spectra area along temperature and point out no magnetic signal near T$_N$ ∼ 240 K for both samples. Thus, the instrumental resolution achieved let us confirm a similar transition temperature of the magnetic order.

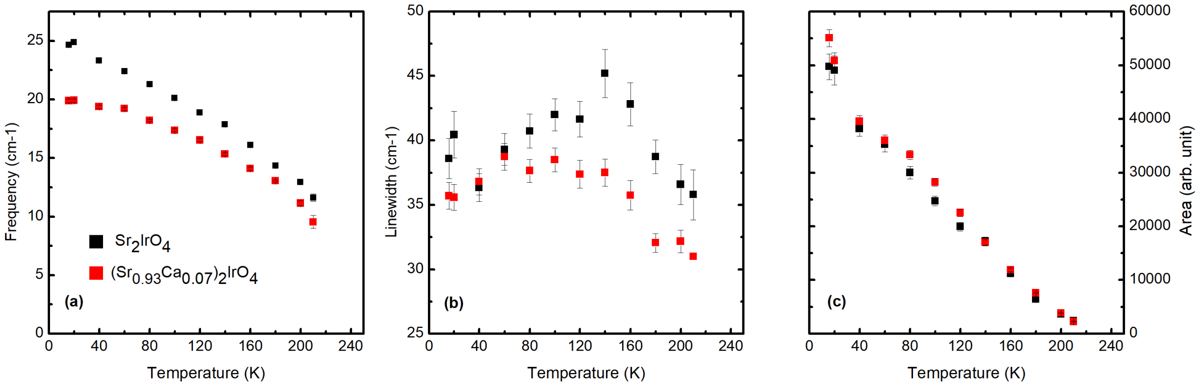

Figure 5.17: Temperature dependence of the (a) magnon frequency, (b) linewidth, and (c) area of the single magnon spectra for the following samples: Sr$_2$IrO$_4$, (Sr$_0$.93Ca$_0$.07)$_2$IrO$_4$

Chapter 6

Discussion

Potential new forms of superconductivity or a competition of novel exotic ground states attracted the researchers' attention to the spin-orbit coupled Mott insulator Sr_2IrO_4. High-pressure studies showed an avoided metallization state and anomalous behavior on the insulate state with a coexistence of different magnetic order domains or other possible competing orders [22, 25, 26]. In this way, our study about Sr_2IrO_4 under chemical pressure has focused on the correlation of its structure, magnetic order, and their low energy excitations. Surprisingly, the results (chapter 5) showed anomalous behavior not trivially related to the "chemical pressure" or volume tuning.

The characterization and synthesis of our samples with ion substitution into the Sr_2IrO_4 system implied a low miscibility limit of $\sim 10\%$ for Ca or Ba at Sr site. The chemical pressure was able to compress or expand the lattice in accordance to the concentration with these ions of different radii. The equivalent hydrostatic pressure applied relative to the changed unit cell volume was around of ±12 kbar.

Furthermore, we also introduced at sec. 2.2 a theoretical study by Jackeli *et. al.* which it stood that the canting angle of the magnetic moment ($\phi = 13°$) would be related to the DM anisotropy exchange, and this magnetic tilt would be locked to the IrO_6 octahedra rotation along c axis ($\alpha = 11°$) with a positive tetragonal distortion (see fig. 6.1). Thus, we expected that the adjusted unit cell volume would accordingly tune the coupled canting magnetic moment and the Ir-O-Ir angle in conjunction. Additionally, the adjusted Ir-O bond lengths and ion substitution would tune the phonon energies as the volume changes. However, our magnetic and Raman results show anomalous behavior which could not be directly related to the volume change and the expected Ir-O-Ir angle tuning effect. These anomalous results suggest possible modifications of the strong spin-orbit coupled state $J_{eff} = 1/2$ whose lattice and magnetic degrees of freedom cooperate to stabilize the observed properties.

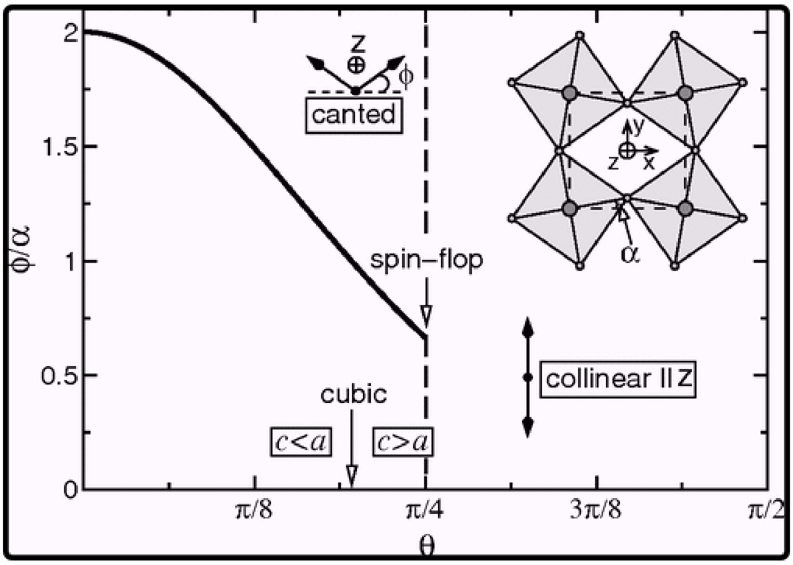

Figure 6.1: Schematic representation of the 'compass model' relating the spin canting angle ϕ in units of the oxygen octahedra rotation angle α as a function of the tetragonal distortion parameter θ. In the cubic case, we have $\phi = \alpha$. In case of a increased tetragonal distortion (c $>$ a) the canting angle is reduced ($\phi/\alpha < 1$). In addition, the spin-flip transition to a collinear AFM ordering along c axis occurs at $\theta = \pi/4$. *Figure and caption adapted from ref.* [6].

In order to clarify this point, we discuss the local and magnetic anomalous results according to isovalent atomic substitutions. The table 6.1 shows an estimation of the canting angle ϕ and the relation ϕ/α using as a reference the parent sample's properties and the magnetic moment obtained for each sample as illustrated in our results (figure 5.6). Additionally, we contrast the magnetic excitation M_0 behavior with a previous theoretical study about the pseudospin-lattice coupling of the ground system Sr_2IrO_4.

6.1 Samples with concentration of Ca

Particularly, the sample with 2% of Ca at Sr site have showed a higher reduction of the a,b than c cell parameter, an anomalous $\sim$ 10% reduction of the parent's canted magnetic moment, and a slight transition temperature reduction of $\sim$ 2.9%. In sec. 2.2, we

	Magnetic moment M_{FC} (μ_B/Ir)	$\phi° = \arcsin(\frac{M_{FC} \times \sin(11)}{M_{ref}})$	ϕ/α
Ca 2%	0.0414 (2)	9.9°	0.9
Ca 5%	0.0307 (9)	7.4°	0.67
Ca 7%	0.0213 (2)	5.1°	0.46
Ca 10%	0.0336 (7)	8.1°	0.74
Ba 5%	0.0265 (2)	6.3°	0.57
Ba 10%	0.0275 (2)	6.6°	0.6

Table 6.1: Estimation of the canting angle ϕ and the relation ϕ/α using FC Magnetization mode results at T = 2 K (figure 5.6) and the parent sample Sr_2IrO_4 magnetic moment as a reference with $M_{ref} = 0.0457(\mu_B/\text{Ir})$ and an angle $\alpha = 11°$ (Ir-O-Ir angle).

mentioned Dzyaloshinskii-Moriya interaction is responsible for the net magnetic moment in the parent sample that is correlated to the octahedra rotation of IrO_6 ($\alpha = 11°$) around the c axis, although, there is a slight misalignment with the magnetic tilting angle $\phi = 13°$. Thus, the reduced volume seems unlikely to reduce the structural and magnetic rotation together where the reduced hypothetical canting angle would be $\phi \sim 9.9$ for the sample with 2% of Ca (table 6.1). The Raman spectra showed similar phonon linewidths with respect the parent sample with an indication of small disorder caused by the chemical substitution, however, the phonon mode M_4 showed an abruptly reduced energy and phonon mode M_2 also showed an intermediate softening above T_N, where the pseudospin-phonon coupling would not influence phonon's energy. Thus, the faster ab plane reduction than the c axis could have increased the tetragonal distortion which would reduce the ϕ/α relation as pictured in fig. 6.1 [6]. The increased tetragonal distortion could have a strong softening effect at their apical mode M_4 and could also reduce the magnetic canting angle ϕ while the octahedra rotation α might increase slightly or not.

Samples with 5% and 7% of Ca also showed a reduction of the magnetic moment canting, for which the ϕ angle would be hypothetically reduced to $\sim 7.4°$, and $\sim 5.1°$, respectively (table 6.1). The reduced octahedra rotation angle α for a compressed volume cell brought back again the thought of a possible reduced relation ϕ/α with a higher tetragonal distortion Δ. Taking into consideration a reasonable slight higher octahedra rotation α, these both samples could be near the limit of the spin-flop transition. In the same line, the sample with 10 % of Ca would also be near the limit of the spin-flop transition and those samples could show a coexistence of the canted and the collinear AFM state.

Moreover, the presence of higher pseudospin-phonon coupling on modes M_2 - M_4 compared to the parent sample shows a tuning effect to the octahedra environment that favors the coupling. In addition, the covalency character that Ca-O presents could be another possible way to tune the tetragonal crystal field and the softening of the octahedra rotation α [56, 57, 58]. Thus, the complex extended multiorbital features of the $J_{eff} = 1/2$ pseudospin and their correlation with the lattice geometry need further studies to understand their degrees of freedom and their exchange interaction.

6.2 Samples with concentration of Ba

The synthesized samples for 5% and 10% of Ba at Sr site have expanded the unit cell volume, as an applied negative pressure. The cell expansion showed an anisotropic increment compared to the parent sample with a higher $\%\Delta c/c = 0.10(4)$ to a $\%\Delta a/a = 0.03(6)$ for the sample with 5% of Ba, and a $\%\Delta c/c = 0.25(7)$ to a $\%\Delta a/a = 0.18(2)$ for the sample with 10% of Ba. Then, we observed a decreased canting moment which would be approximately equivalent to $\phi \sim 6.3°$ and 6.6°, for the samples with 5% and 10% of Ba, respectively (table 6.1). However, if it is not accompanied with a reduced octahedra rotation α, the relation ϕ/α may also be near the spin-flop transition limit as the samples with Ca. On the other hand, an expansion of the unit cell favors to reduce α.

Furthermore, stronger pseudospin-phonon coupling in the optical phonons M_2-M_4 demonstrates the sensibility of a new configuration around the $J_{eff} = 1/2$ that favors the magnetic coupling below T_N. In the same line, a higher electronic continuum interference (1/q) and a reduced anharmonic parameter related to the rotation IrO_4 mode (M_2) have shown evidence that the local distortions with Ba substitutions open a channel to induce carrier fluctuations at their ground state.

6.3 Magnetic excitation M_0 above chemical pressure

A theoretical study stood that an orthorhombic instability at $T_{JT} \approx T_N$ and a lattice-pseudospin coupling would be responsible to own magnetic domains with an easy along a or b axis. This anisotropic interaction would be also essential to stabilize the magnetic order state at T_N [7]. The figure 6.2 shows an schematic representation of the

Jahn-Teller (JT) Orbital-lattice coupling and the analogous mechanism of the pseudospin-lattice coupling for the strong spin-orbit system with $J_{eff} = 1/2$. There, the lattice geometry distortion, the pseudospin-lattice coupling and the interactions hierarchy along the system Sr_2IrO_4 establish the magnitude of this low energy gap as $\omega_{M_0} = 8S\sqrt{J\Gamma_1}$, where Γ_1 is the pseudospin-lattice parameter for the orthorhombic distortion along a or b axis. The pseudospin-lattice parameter accounts the following expression: [7]

$$\Gamma_1 = \varepsilon_1(t^2/U)(\sin^2 2\theta/E_{BA})(J_H/U), \tag{6.1}$$

where, $\varepsilon_1, t, U, E_{BA}, J_H, \theta$ are orthorhombic deformation, hopping amplitude, Coulomb repulsion, energy difference from state A and B at fig. 6.2 ($E_{BA} \sim 3/2\lambda$), Hund's coupling, and parameter of tetrahedral distortion, respectively.

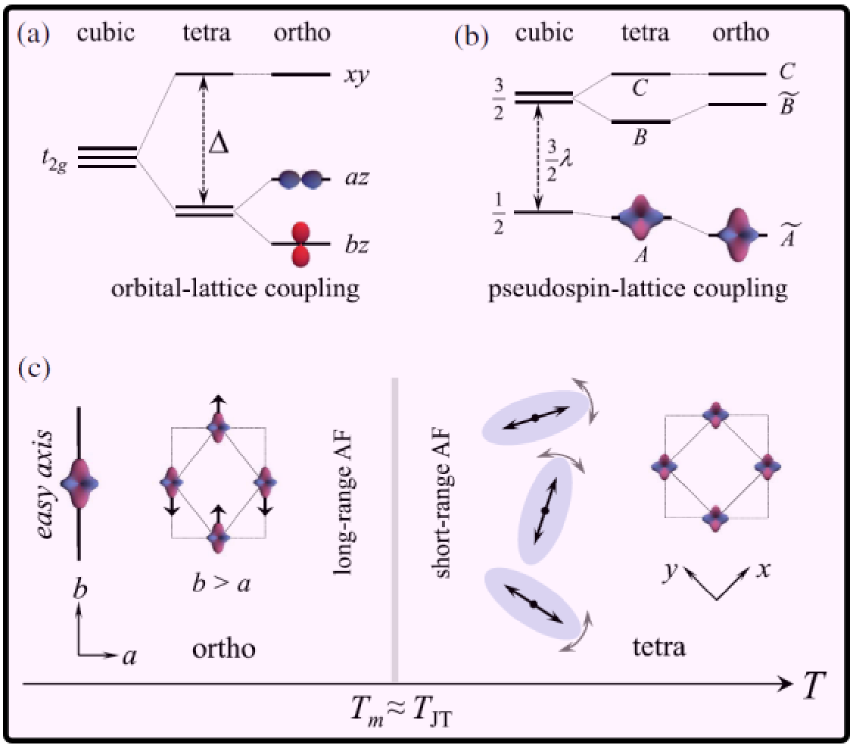

Figure 6.2: t_{2g} hole multiplet structure under cubic, elongated tetragonal (c¿a), and orthorhombic crystal fields for a system (a) without SOC and (b) with SOC (corresponds to the Sr_2IrO_4 system). (c) The orthorhombic deformation b ¿ a enhances $|\pm 1, \pm\frac{1}{2}\rangle$ pseudospin wave functions via Jahn Teller interaction (pseudospin-lattice interaction). Thus, selecting b axis for the moment direction, below T_{JT} a long range AFM order develop. *Figure and caption adapted from ref.* [7].

In addition, a previous Raman study of this spin gap under physical pressure observed an split of 2 cm^{-1} ($\omega_{M_0} \sim 20$), which was ascribed to possible cell distortions inhomogeneous strain distribution causing two domain regions at the sample [59]. However, moderate applied pressures applied P $\sim 1.8 - 26$ kbar did not show a gap energy-pressure dependence.

Bearing in mind the theoretical study and the previous experimental result under physical pressure, the tuned volume might not have a direct influence to the magnetic excitation energy ω_{M_0}. In contrast, the single magnon M_0 of our samples under chemical pressure did not show an split with even narrower linewidths at low temperature. This would imply homogeneous distributed magnetic domains for our polycrystalline sample. Furthermore, the reduced energy gap for our samples under isovalent substitutions could indicate a reduced orthorhombic instability.

In addition, at the pseudospin-lattice equation 6.1, there is a relative maximum for a tetragonal distortion parameter at $\theta = \pi/4$ near the spin-flop transition that would be achieved in accordance to these studies [6, 7]. Our results show us this single magnon gap remains nearly to $\omega_{M_0} = 17$ cm^{-1} (5 cm^{-1} lower from the parent sample's). This open the question if an increment of tetragonal distortion Δ, would be also correlated to this reduced orthorhombic instability.

Figure 6.3 shows a projection of the plane SrO above IrO_2. There, Sr site has coordination with 9 Oxygen atoms, where 5 O^{-2} atoms are distributed one at adjacent plane and four at the SrO plane with 4/m symmetry. The remaining 4 O^{-2} occupy a lower symmetry site 2/m (sensible to suffer distortions) at the IrO_2 plane where the octahedra IrO_6 is rotated α. Thus, the isovalent substitution with Ca or Ba might adjust locally different along their bond lengths and/or Ir-O-Ir angle at IrO_2 plane in comparison to the Ir-O bond length along c axis, and the crystal field around $J_{eff} = 1/2$.

Taking our analysis and previous studies into account, tuning the lattice degrees of freedom of Sr_2IrO_4 system by local distortions with isovalent chemical susbtitutions at Sr site have probed tetragonal crystal field changes at their optical phonons and a reduced octahedra instability of the quasi-2D single layered iridate at the single magnon excitation.

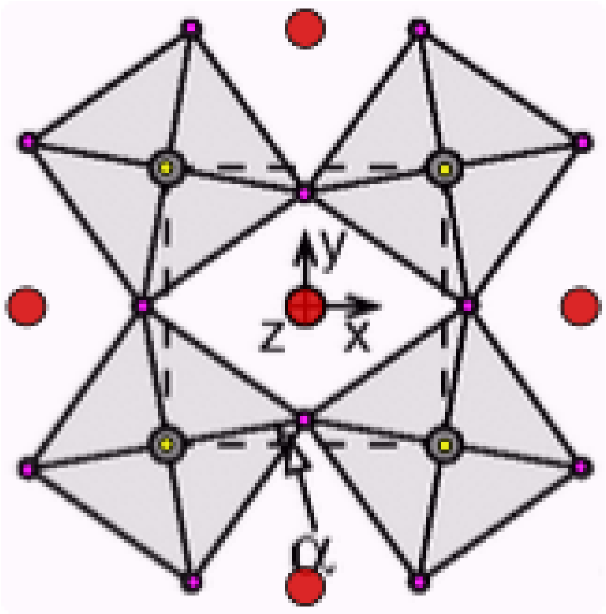

Figure 6.3: Projection of the SrO plane at the xy plane, where Sr^{+2} and O^{+2} ions at the same plane are represented respectively with red and yellow circles. O^{+2} ions of the IrO_2 plane are represented with fuchsia circles.

Chapter 7

Conclusion

Novel phenomena that combine the influence of strong spin-orbit coupling and moderate electron correlations have brought the scientific community's attention to understand the new physics be presented by Sr_2IrO_4 and the family of iridates. Exotic properties due to electron doping or above high pressure have shown signals related to such states as a possible novel superconductivity or a highly frustrated quantum magnetic state, respectively [19, 26]. Thus, understanding the details of Sr_2IrO_4 via external parameters is important for a realistic description.

This work was focused on the Sr_2IrO_4 iridate under chemical pressure. The synthesized polycrystalline samples of the series $(Sr_{1-x}A_x)_2IrO_4$ with A = (Ca, Ba) ion substitution showed a similar low miscibility limit with $\sim$ 10% concentration for Ca or Ba at Sr site. The systematic study of the samples by Raman scattering, X-ray diffraction, and DC-magnetization techniques showed properties that agree with a good crystalline quality and an stable long range magnetic order with a similar transition temperature $T_N \sim 237$ K [60]. In addition, the chemical pressure was able to tune the unit cell volume, the net magnetic moment and their low energy excitations, however, the change of their magnetic properties and low energy excitations was not directly related to the compression or expansion of the unit cell.

The anomalous results indicate allusive crystal environment changes around the strong spin-orbit coupled $J_{eff} = 1/2$ state that enhanced the pseudospin-phonon coupling (M_3-M_4)) and a continuum electronic phonon coupling (M_2). Particularly, the magnetic and their low energy excitations properties showed the important role of the lattice degrees of freedom that play to stabilize the collective spin-orbital state $J_{eff} = 1/2$ and their long range magnetic order below T_N.

Bibliography

[1] W. Witczak-Krempa, Gang Chen, Y. Baek Kim, L. Balents, Annu. Rev. Condens. Matter Phys. **5** 57–82 (2014).

[2] Jeffrey G. Rau, Eric Kin-Ho Lee, Hae-Young Kee, Annu. Rev. Condens. Matter Phys. **7** 195–221 (2016).

[3] B. J. Kim, H. Jin, S. J. Moon, J. Y. Kim and B. G. Park, Phys. Rev. Lett. **101**, 076402 (2008).

[4] J. Bertinshaw, G. Khaliullin, B. J. Kim, Y. K. Kim, Annu. Rev. Condens. Matter Phys. , **10** 315-336 (2019).

[5] Keimer, B., Kivelson, S., Norman, M. Nature **518**, 179–186 (2015)

[6] G. Jackeli and G. Khaliullin, Phys. Rev. Lett. **102**, 017205 (2009).

[7] Liu, Huimei and Khaliullin, Giniyat, Phys. Rev. Lett. **122** 5, 057203 (2019).

[8] Gang Cao and Pedro Schlottmann, Rep. Prog. Phys. **81** 042502 (2018).

[9] B. J. Kim, H. Ohsumi, T. Komesu, S. Sakai, T. Morita, H. Takagi, and T. Arima, Science **323**, 5919 (2009).

[10] M. Crawford, M. Subramanian, R. Harlow, J. Fernandez-Baca, Z. Wang and D. Johnston, Phys. Rev. B **49**, 9198-9201 (1994).

[11] Q. Huang, J.L. Soubeyroux, O. Chmaissem, I. Natali Sora, A. Santoro, R.J. Cava, J.J. Krajewski, W.F. Peck, J. Solid State Chem. **112**, 355-361 (1994).

[12] F. Ye, S. Chi, B. C. Chakoumakos, J. A. Fernandez-Baca, T. Qi and G. Cao, Phys. Rev. B **87**, 140406(R) (2013).

[13] L. Zhao, D. H. Torchinsky, H. Chu, V. Ivanov, R. Lifshitz, R. Flint, T. Qi, G. Cao and D. Hsieh, Nat. Phys. **12**, 32-36 (2016).

[14] C. Dhital, T. Hogan, Z. Yamani, C. de la Cruz, X. Chen, S. Khadka, Z. Ren, and S. D. Wilson, Phys. Rev. B **87** 144405 (2013).

[15] J. G. Vale, S. Boseggia, H.C. Walker, R. Springell, Z. Feng, E. C. Hunter, R. S. Perry, D. Prabhakaran, A. T. Boothroyd, S. P. Collins, H. M. Ronnow, and D. F. McMorrow, Phys. Rev. B **92** 2, 020406 (2015).

[16] H. Gretarsson, J. Sauceda, N. H. Sung, M. Höppner, M. Minola, B. J. Kim, B. Keimer, and M. Le Tacon, Phys. Rev. B **96** 115138 (2017).

[17] Y. Gim, A. Sethi, Q. Zhao, J. F. Mitchell, G. Cao and S. L. Cooper, Phys. Rev. B **93** 024405 (2016).

[18] Porras, J. and Bertinshaw, J. and Liu, H. and Khaliullin, G. and Sung, N. H. and Kim, J.-W. and Francoual, S. and Steffens, P. and Deng, G. and Sala, M. Moretti and Efimenko, A. and Said, A. and Casa, D. and Huang, X. and Gog, T. and Kim, J. and Keimer, B. and Kim, B. J., Phys. Rev. B **99** 8, 085125 (2019).

[19] J. Kim, M. Daghofer, A. Said, T. Gog, J. van den Brink, G. Khaliullin and B. J. Kim, Nat. Commun. **5**, 4453 (2014).

[20] S. J. Moon, H. Jin, K. W. Kim, W. S. Choi, Y. S. Lee, J. Yu, G. Cao, A. Sumi, H. Funakubo, C. Bernhard, and T. W. Noh, Phys. Rev. Lett., **101**, 226402 (2008).

[21] K. Samanta, D. Rigitano, P. G. Pagliuso, and E. Granado, Appl. Phys. Lett. **114** 152402 (2019).

[22] K. Samanta, F. M. Ardito, N. M. Souza-Neto, and E. Granado, Phys. Rev. B **98** 094101 (2018).

[23] K. Samanta, R. Tartaglia, U. F. Kaneko, Souza-Neto N. M., and E. Granado, Phys. Rev. B **101** 075121 (2020).

[24] C. Chen, Y. Zhou, X. Chen, T. Han, C. An, Y. Zhou, Y. Yuan, B. Zhang, S. Wang, R. Zhang, L. Zhang, C. Zhang, Z. Yang, Lance E. DeLong, and G. Cao, Phys. Rev. B **101** 14, 144102 (2020).

[25] D. Haskel, G. Fabbris, M. Zhernenkov, P. P. Kong, C. Q. Jin, G. Cao and M. van Veenendaal, Phys. Rev. Lett. **109** 2, 027204 (2012).

[26] Haskel, D. and Fabbris, G. and Kim, J. H. and Veiga, L. S. I. and Mardegan, J. R. L. and Escanhoela, C. A. and Chikara, S. and Struzhkin, V. and Senthil, T. and Kim, B. J. and Cao, G. and Kim, J.-W., Phys. Rev. Lett. **124** 6, 067201 (2020).

[27] U. Fano, Phys. Rev. **124** 1866-1878 (1961).

[28] W. Hayes, R. Loudon, **Scattering of light by crystals**. Dover Publications (2004).

[29] M. Cardona (Ed.), **Light Scattering in Solids I: Introductory Concepts** Topics Appl. Phys., Vol. 8. Springer, Berlin (1982).

[30] M. Cardona, G. Güntherodt (Eds.), **Light Scattering in Solids II: Basic Concepts and Instrumentation**, Topics Appl. Phys., Vol. 50. Springer, Berlin (1982).

[31] M. Cardona, G. Güntherodt (Eds.), **Light Scattering in Solids VII: Crystal Field and Magnetic Excitations**, Topics Appl. Phys., Vol. 75. Springer, Berlin (2000).

[32] J. R. Ferraro, K. Nakamoto. **Introductory Raman Spectroscopy**. Academic Press (1994).

[33] L. D. Landau, E. M. Lifshitz, *Statistical Physics. Vol. 5 of Course of Theoretical Physics (2nd ed.)*. Pergamon Press (1970).

[34] M. Born and K. Huang, *Dynamical Theory of Crystal Lattices*, Clarendor Press (1954).

[35] W. Cochran, *The Dynamics of Atoms in Crystals*, Edward Arnold (1973).

[36] J. A. Reissland, *The Physics of Phonons*, Wiley (1973).

[37] N. Ashcroft and N. D. Mermin, *Solid State Physics*, Saunders College Publishing (1976).

[38] M. Balkanski, R. F. Wallis and E. Haro, Phys. Rev. B **28** 1928-1934 (1983).

[39] R. A. Cowley, J. Phys. France **26**, 659-667 (1965).

[40] P. G. Klemens, Phys. Rev. **148** 845 (1965).

[41] W. Baltensperger, J. S. Helman, Helv. Phys. Acta **41**, 668 (1968).

[42] E. Granado, A. García, J. A. Sanjurjo, C. Rettori, I. Torriani, F. Prado, R. D. Sánchez, A. Caneiro, and S. B. Oseroff, Phys. Rev. B **60** 17, 11879-11882 (1999).

[43] Eduardo Granado, *Estudos de propriedades ópticas e magnéticas de manganitas* [Tese de Doutorado, Universidade Estadual de Campinas] Repositório da Produção Científica e Inteletual da Unicamp, https://doi.org/10.47749/T/UNICAMP.2000.184492 (2000).

[44] A. R. West, **Solid state Chemistry and its Applications, 2nd Edition**. John Wiley and Sons (2014).

[45] B. Toby, J. Appl. Crystallogr. **34**, 210-213 (2001).

[46] G. Cao, J. Bolivar, S. McCall, J. Crow and R. Guertin, Phys. Rev. B **57** 11039-11042 (1998).

[47] B. D. Cullity, C. D. Graham, **Introduction to Magnetic Materials, 2nd Edition**. Jhon Wiley and Sons (2009).

[48] X. Chen and S. D. Wilson, Phys. Rev. B **94** 195115 (2016).

[49] P. Thompson, D. E. Cox, and J. B. Hastings, J. Appl. Cryst. **20** 79-83 (1987).

[50] G. Zhou, X. Gu, X. Yang, X. Gao, K. Wang, J. Peng, F. Zhang and X. S. Wu, AIP Adv. **7** 055823 (2017).

[51] R. Cava, B. Batlogg, K. Kiyono, H. Takagi, J. Krajewski, W. Peck, L. Rupp, and C. Chen, Phys. Rev. B **49** 11890-11894 (1994).

[52] M. Ge, T. F. Qi, O. B. Korneta, D. E. De Long, P. Schlottmann, W. P. Crummett, and G. Cao, Phys. Rev. B **84** 100402 (2011).

[53] T. Shimura, Y. Inaguma, T. Nakamura, and M. Itoh, Y. Morii, Phys. Rev. B **52** 13 (1995).

[54] T. Han, D. Lian, Y. Wang, J. Yang, H. Han, J. Wang, J. Gong, L. Luo, W. K. Zhu, C. Zhang and Y. Zhang, J. Supercond. Nov. Magn. **30** 3493-3496 (2017).

[55] J. Menéndez, and M. Cardona, Phys. Rev. B **29** 2051-2059 (1984).

[56] R. D. Shannon, Acta Cryst. A **32**, 751-767 (1976).

[57] K. Maiti, Phys. Rev. B **73**, 235110 (2006).

[58] R. Shankar Singh and K. Maiti, arXiv:cond-mat/0605552 (2006).

[59] Yewon Gim, *Beyond the isotropic two-dimensional Heisenberg Model: Raman scattering studies of the transition between isotropic and anisotropic spin dynamics in* Sr_2IrO_4, [Doctoral dissertation, University of Illinois] Illinois Library, https://hdl.handle.net/2142/101467 (2018).

[60] N. H. Sung, H. Gretarsson, D. Proepper, J. Porras, M. Le Tacon, A. V. Boris, B. Keimer and B. J. Kim (2016), Philosophical Magazine, **96** 4, 413-426 (2016).